



THE UNIVERSITY OF QUEENSLAND

Characterization of Micro-Scale Flow and Induced Contact Erosion

Student Name: Yingyi ZHANG

Course Code: ENGG7282

Supervisor: Associate Professor Alexander Scheuermann
Dr Mohammad Aminpour

Submission date: 30 May 2019

Faculty of Engineering, Architecture and Information Technology

Abstract

Hydraulically loaded soil structures such as embankments and dams may be subjected to contact erosion. Contact erosion happens at the interface between soil layers formed by soil particles of different sizes, and is triggered by external flows applied to the soil layers. In classical contact erosion investigations, the external flows were assumed to be uniform. In the presented experimental study, this external flow was disturbed by the expansion effect. The expansion effect happens when pipe flows travel through a sudden-expanding cross-section. The first part of the study tried to stabilize the disturbance in flow regimes caused by the expansion effect. Micro-scale flow regimes influenced by the expansion effect were measured and characterized under different conditions configured by flow rates, porous screens, and the insertion of a granular medium. The disturbance was found to be stabilized by placing a porous screen at the expanding plane, or by increasing the flow rate. The insertion of a granular medium also influenced flow regimes. The findings helped optimize the experimental setup for studying contact erosion, and allowed a uniform flow to be applied to the testing section. Micro-scale flows at the interface between two layer of particles of different sizes were then studied. The critical pore flow speed to trigger contact erosion was investigated, and was found to be influenced by different pore and particle configurations. The findings can provide new ideas in improving stability of soil structures subjected to contact erosion.

Acknowledgement

I would like to express my special thanks to my parents and my partner, Yizhou Liu, for their endless unconditional support. They gave me invaluable emotional and financial support in finishing my master degree.

I express my deepest and sincerest gratitude to my two supervisors: Associate Professor Alexander Scheuermann and Dr Mohammad Aminpour. Associate Professor Alexander Scheuermann gave me invaluable advice on my research and in writing this thesis. I would like to thank him a lot for being patient with me during this thesis project, and for offering me a PhD opportunity. I also would like to give much thanks to Dr Mohammad Aminpour for helping me in designing experiments, coding for data processing, and academic writing. My first conference abstract has been published with great help from him. My first journal paper in progress also received huge support from Dr Mohammad Aminpour. My two supervisors guided me into this fascinating world of research.

I would like to thank The University of Queensland for providing me with the best environment for successfully completing all the works for the thesis. Technicians at the UQ Geotechnical Engineering Centre provided huge support for the experiments.

Keywords

Contact erosion, Expansion effect, PIV (particle image velocimetry) technique, Flow characterization

Table of Contents

Abstract	i
Acknowledgement	ii
Keywords	iii
Table of Contents	iv
List of Figures	vi
Abbreviations	viii
1 Introduction.....	1
2 Literature Review.....	2
2.1 Contact erosion	2
2.1.1 Significance.....	2
2.1.2 Field-scale studies on contact erosion.....	3
2.1.3 Micro-scale studies on contact erosion	4
2.1.4 Flows in granular media.....	7
2.2 Particle image velocimetry (PIV) technique.....	9
2.2.1 Tracer particles.....	9
2.2.2 Light source.....	10
2.2.3 Refractive index matching (RIM) methods	11
2.2.4 Image processing.....	11
2.3 Expansion effect.....	12
2.3.1 Significance.....	12
2.3.2 Flow characterization in expansion effect	13
2.3.3 Expansion effect mitigation	14
3 Scope of Project	14
3.1 Statement of problems	14
3.2 Objectives	15
4 Methodology	15

4.1 Experimental setup	15
4.1.1 Water circulation system and testing section	15
4.1.2 PIV system.....	17
4.2 Experimental procedure.....	18
4.2.1 Experiments for expansion effect	18
4.2.2 Experiments for contact erosion initiation.....	21
5 Results and Discussion	23
5.1 Expansion effect: disturbance and stabilization	23
5.1.1 Velocity distribution in empty chamber	23
5.1.2 Velocity distribution in granular medium	28
5.1.3 Quantitative study of disturbed flow regime	32
5.1.4 Limitations of the study	36
5.2 Contact erosion initiation	37
5.2.1 Experimental setup	37
5.2.2 Normalization of velocity data	38
5.2.3 Variation in initiating flow speed	42
5.2.4 Limitations of the study	46
6 Conclusions and Recommendations	47
References	49
Appendices: Result Tables	55

List of Figures

Fig. 2-1 A simulated contact erosion process, shown in time sequence from left to right (Galindo-Torres <i>et al</i> , 2015)	3
Fig. 2-2 Experimental setup for a field-scale study on contact erosion (Ho, 2007)	4
Fig. 2-3 The evolution of pore structure under (a) Triaxial compression; and (b) Triaxial extension (Chang and Zhang, 2012)	5
Fig. 2-4 The rotating particles, shown in time sequence from left to right (Brumby et al, 2015)	5
Fig. 2-5 (a) Numerical model for simulating contact erosion initiation; (b) Definition of parameters; (c) Initiating flow speed normalized with the Froude number versus L_p / D_b ; (d) Jet-like flow pattern at the top of the fine particle bed (Harshani, 2017)	6
Fig. 2-6 Experimental setup for a micro-scale study on contact erosion (Beguin, Philippe and Faure, 2012)	7
Fig. 2-7 Vortices at the back side of a sphere confronted with viscous flow, when (a) $Re = 37.7$; and (b) $Re = 73.6$ (Taneda, 1956)	8
Fig. 2-8 (a) Hydro-gel beads suspended in air; and (b) Hydro-gel beads submerged in water (Weitzman et al, 2014).....	12
Fig. 2-9 Reverse streamlines and vortices caused by the expansion effect (Hertzberg and Ho, 1995)	12
Fig. 4-1 (a) Schematic drawing; and (b) Photograph of the experimental setup.....	16
Fig. 4-2 Testing section dimensions and division, filled with hydro-gel beads	17
Fig. 4-3 Porous screen conditions in Group A, Group B, D, and Group C, E (a) No porous screen; (b) 5-mm-diameter coarse glass beads screen; and (c) 1-mm-diameter fine glass beads screen	20
Fig. 4-4 Force analysis of a base particle when (a) A tangential flow is applied (Abdelhamid and El Shamy, 2014); and (b) A vertical flow is applied	21
Fig. 5-1 Vector field graphs for different experimental configurations: (a) Group A, empty chamber with no porous screen; (b) Group B, empty chamber with coarse glass beads screen; and (c) Group C, empty chamber with fine glass beads screen. With upwards velocity plotted in blue and downwards velocity plotted in magenta. Applied flow rates from left to right: for Group A and B, 0.1 lit/min ($Re_c = 16.67$), 1 lit/min ($Re_c = 166.67$), 2 lit/min ($Re_c = 333.33$), 4 lit/min ($Re_c = 666.67$), and 8 lit/min ($Re_c = 1333.33$); for Group C, 0.1 lit/min, 1 lit/min, 2 lit/min, 4 lit/min, and 5 lit/min ($Re_c = 833.33$)	24
Fig. 5-2 PDF plotting of flow-wise velocity components in the middle section at different applied flow rates for (a) Group A, empty chamber with no porous screen; (b) Group B, empty	

chamber with coarse glass beads screen; and (c) Group C, empty chamber with fine glass beads screen.....	26
Fig. 5-3 Vector field graphs for different test configurations: (a) Group D, granular medium with coarse glass beads screen; and (b) Group E, granular medium with fine glass beads screen. With upwards velocity plotted in blue and downwards velocity plotted in magenta. Applied flow rates from left to right: for Group D, 0.1 lit/min ($Re_m = 3$), 1 lit/min ($Re_m = 30$), 2 lit/min ($Re_m = 60$), 4 lit/min ($Re_m = 120$), and 8 lit/min ($Re_m = 240$); for Group E, 0.1 lit/min, 1 lit/min, 2 lit/min, 4 lit/min, and 5 lit/min ($Re_m = 150$)	28
Fig. 5-4 PDF plotting of flow-wise velocity components in the middle section at different applied flow rates for (a) Group D, granular medium with coarse glass beads screen; and (b) Group E, granular medium with fine glass beads screen	29
Fig. 5-5 PDF plotting of flow-wise velocity components in the middle section with different experimental configuration at the applied flow rate of (a) $q = 0.1$ lit/min; and (b) $q = 4$ lit/min	32
Fig. 5-6 Tortuosity versus applied flow rate for different experimental configuration at the (a) Entrance section; and (b) Middle section of the chamber; (a) and (b) share the same legend.	33
Fig. 5-7 Reverse flow velocity ratio versus applied flow rate for different experimental configuration at the (a) Entrance section; and (b) Middle section of the chamber; (a) and (b) share the same legend	35
Fig. 5-8 Velocity vector field graph generated with PIVView 2C, showing velocity vectors (green arrows), filter particles (blue solid circles) and base particles (gray solid circles)	38
Fig. 5-9 (a) An inclined top view; and (b) A PIV system's view of filter particles (blue sphere), base particles (red sphere), and the light sheet (white plane).....	38
Fig. 5-10 Fr_{int} versus u_f for different geometrical configurations in the range of u_f results.....	43
Fig. 5-11 C_D versus Re_p in the range of Re_p results.....	43
Fig. 5-12 Fr_{int} variation for different geometrical configurations.....	44
Fig. 5-13 (a) An inclined top view; (b) a top view; and (c) A PIV system's view of filter particles (blue sphere), base particles (red sphere), and the light sheet (white plane)	46

Abbreviations

CCD charge-coupled device

CFD computational fluid dynamics

FOV field of view

IW interrogation window

LED light-emitting diode

PDF probability density function

PIV particle image velocimetry

PSP Polyamide seeding particle

RIM refractive index matching

1 Introduction

Contact erosion is a form of soil corrosion that happens at the interface between two soil layers formed by soil particles of different sizes. When an external flow applied to the soil layers is high enough to overcome the adhesion and friction force between fine soil particles, the fine soil particles will dislodge from their original layer, and travel into the coarse-particle soil layer through pores between adjacent coarse particles. As fine soil particles constantly dislodge, a mass loss occurs at the fine-particle soil layer. The shear strength of the soil body therefore decreases (Beguin, Philippe and Faure, 2012). Contact erosion threatens hydraulically loaded soil structures, such as embankments and dams (Galindo-Torres *et al*, 2015). The decreased shear strength caused by contact erosion makes failures more likely to occur, and therefore poses threats to properties and people in the neighborhood (Foster, Fell and Spannagle, 2000). Therefore, it is important to study contact erosion in improving stability of such soil structures. Yet, the current knowledge about the triggering mechanism of contact erosion is limited.

Previous studies indicated the importance of studying contact erosion at a micro scale, as delicate micro-scale deformation and displacement of particles were proven to influence contact erosion outcomes (Chang and Zhang, 2012; Abdelhamid and El Shamy, 2014). This thesis report presents an experimental study on micro-scale flows in granular media that induce contact erosion. Two layers of granular media formed by spheres of two different sizes are placed in a testing chamber to simulate the geometrical arrangement in contact erosion. An external flow is applied to the testing chamber to trigger contact erosion. This study focuses on how different geometrical configurations of spheres influence the critical pore flow speed to trigger contact erosion in local areas. The studied geometrical parameters are different size ratios between fine and coarse spheres, and different size ratios between pore widths and fine sphere diameters. The micro-scale flow speed inside pores between adjacent spheres is measured with the particle image velocimetry (PIV) technique. This experimental study tries to address the research gap in contact erosion initiation at a micro-scale.

In experiments of contact erosion initiation, the testing chamber's geometrical configuration causes the expansion effect: the flow regime becomes disturbed when the flow travels through a sudden-expanding cross-section. The disturbance manifests as vortices and reverse streamlines against the applied flow (Back and Roschke, 1972). This sudden-expansion happens when the external flow applied to the testing chamber travels from a pipe into the chamber through a conical funnel opening. The experiments of contact erosion initiation require uniform flow to be applied as the boundary condition to eliminate impact caused by external variables. Thus, stabilizing the disturbance caused by the expansion effect becomes a secondary

yet prior task in this project. This part of study attempts to stabilize the disturbance by placing porous screens at the expanding plane, or by increasing the flow rate. The impact caused by the insertion of a granular medium on the flow regime influenced by the expansion effect is also studied.

This thesis report is structured as follows:

- In 2 Literature Review, background information is introduced, including key concepts and previous research works relevant to this study
- In 3 Scope of Project, the research problems are stated, and objectives of this study are elaborated
- In 4 Methodology, a detailed experimental method to realize the objectives is introduced; the experimental setup and testing conditions are introduced in detail
- In 5 Results and Discussion, the results are presented, and data processing methods are explained; the experimental results are analyzed both qualitatively and quantitatively; the results are linked back to research works introduced in 2 Literature Review; limitations and further research possibilities are recognized
- In 6 Conclusions and Recommendations, the conclusions and limitations drawn from 5 Results and Discussion are summarized; corresponding recommendations are made to overcome the limitations

2 Literature Review

2.1 Contact erosion

2.1.1 Significance

Multiple soil layers, formed by soil particles of different sizes, are common in soil structures such as embankments and dams (Cyril *et al*, 2009). Hydraulically loaded soil structures with multiple soil layers may be subjected to contact erosion (Galindo-Torres *et al*, 2015). Water flow exerts a hydraulic shear stress to soil particles when it flows through soil layers. When the flow velocity is high enough, the hydraulic shear stress is able to overcome the adhesion and friction forces of fine soil particles. The fine soil particles will then start to dislodge from their original layer, and intrude into the coarse-particle soil layer through the pores between adjacent coarse soil particles (Beguin, Philippe and Faure, 2012). This process is called contact erosion. A simulated contact erosion process is shown in Fig. 2-1.

Contact erosion can lead to catastrophic failures of hydraulically loaded soil structures. As fine soil particles being constantly removed from their original layer, a mass loss occurs. This mass

loss loosens the soil structure, and consequently causes a decrease in its shear strength (Chang, Zhang and Cheuk, 2014). With a lower shear strength, failures are more likely to occur. This poses a great danger to people and properties in the neighborhood of the soil structures subjected to contact erosion (Foster, Fell and Spannagle, 2000). Thus, it is important to study contact erosion for improving stability of hydraulically loaded soil structures.

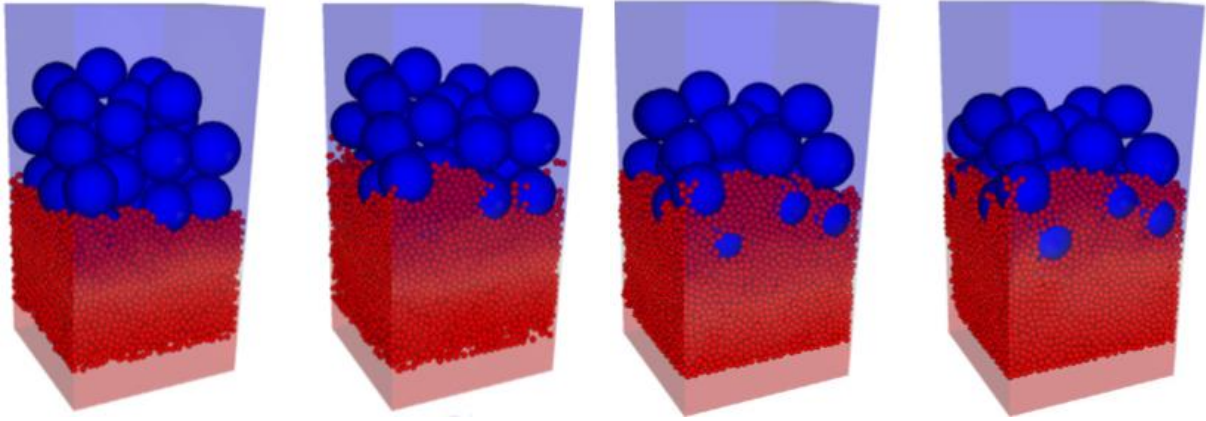


Fig. 2-1 A simulated contact erosion process, shown in time sequence from left to right (Galindo-Torres *et al*, 2015)

2.1.2 Field-scale studies on contact erosion

Many research works about contact erosion were conducted at the field scale through experiments with soil specimens. Cyril *et al* (2009) studied the critical flow velocity to trigger contact erosion with the experimental setup designed by Ho (2007), as shown in Fig. 2-2. In the experiment, two layers of soil with different particle sizes were used, with the fine-particle soil (base-soil) placed below the coarse-soil in the testing system. Contact erosion was triggered by applying a tangential water flow through the soil specimens. The critical flow velocity to trigger contact erosion was recognized as the minimum flow velocity to trigger the soil mass loss. The soil mass loss was identified by a turbidity meter at the outlet of flow. The critical flow velocity was measured for various combinations of base-soil and coarse-soil specimens. The critical flow velocity was found to be related to the porosity of coarse-soil layer and the size of base-soil particles. An empirical equation of the critical flow velocity, q_{cr} , was developed to describe this relationship:

$$q_{cr} = 0.7n_c \sqrt{(S - 1)gD_b \left(1 + \frac{F_c}{F_w}\right)} \quad (2-1)$$

where n_c is porosity of coarse-soil, namely the percentage of void volume in the coarse-soil specimen, S is the specific gravity of base-soil, namely the ratio between base-soil density and water density, D_b is the diameter of base-soil particles, F_c and F_w are the adhesion force and the buoyancy force of base-soil particles respectively.

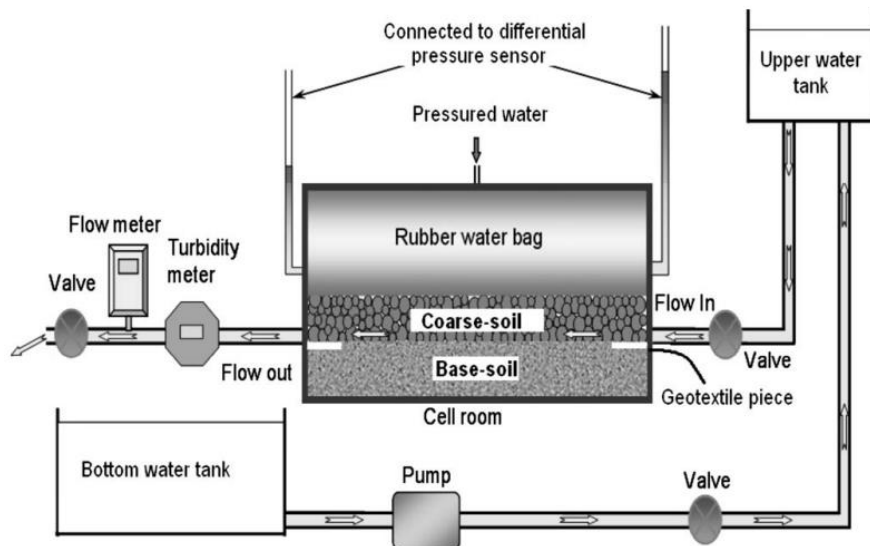


Fig. 2-2 Experimental setup for a field-scale study on contact erosion (Ho, 2007)

In another field-scale study, Chang and Zhang (2012) triggered the soil specimens to erode also by applying an external flow to soil specimens, but the soil specimens were under different stress states. They found that the critical hydraulic shear stress to initiate erosion was higher when the soil specimens were under extension stress conditions than under compression stress conditions. The two stress conditions are illustrated with Fig. 2-3. The researchers concluded that the different states of stress changed the pore structures between soil particles. Thus, it was ultimately the pore structure that influenced the critical hydraulic shear stress. This study indicated the importance of studying contact erosion at a micro scale.

2.1.3 Micro-scale studies on contact erosion

Micro-scale studies allowed soil particles' delicate motion to be studied. Soil particles were found to be rotating when loaded with eccentric forces (Bardet, 1994). This rotation of soil particles was detected in many micro-scale numerical models studying contact erosion, as illustrated with Fig. 2-4. The interaction between a pair of rotating particles was found to cause an upwards movement to the uppermost particle of the pair (Brumby *et al*, 2015). Abdelhamid and El Shamy (2014) constrained the rotation of soil particles in their numerical simulation, and the particles' upwards movement was consequently weakened. In contact erosion, the fine soil particles intrude into the coarse-particle soil layer. As the upwards movement being weakened in the numerical model, the intruding depths of fine soil particles decreased, and contact erosion can therefore be undermined. This rotation linked the micro-scale motion of soil particles to the degree of contact erosion. Considering that the delicate motion of particles can only be observed and studied at a micro scale, this phenomenon indicated the importance of studying contact erosion at the micro scale.

Micro-scale studies also allowed pore velocity to be measured. The pore velocity is the micro-

scale flow velocity in the pores between two adjacent particles in granular media. This pore velocity was measured in different local areas in a numerical model containing layered particles of two different sizes (Galindo-Torres *et al.*, 2015). The numerical results revealed that the pore velocity varied in different zones of the model, where the dominating particle size varied.

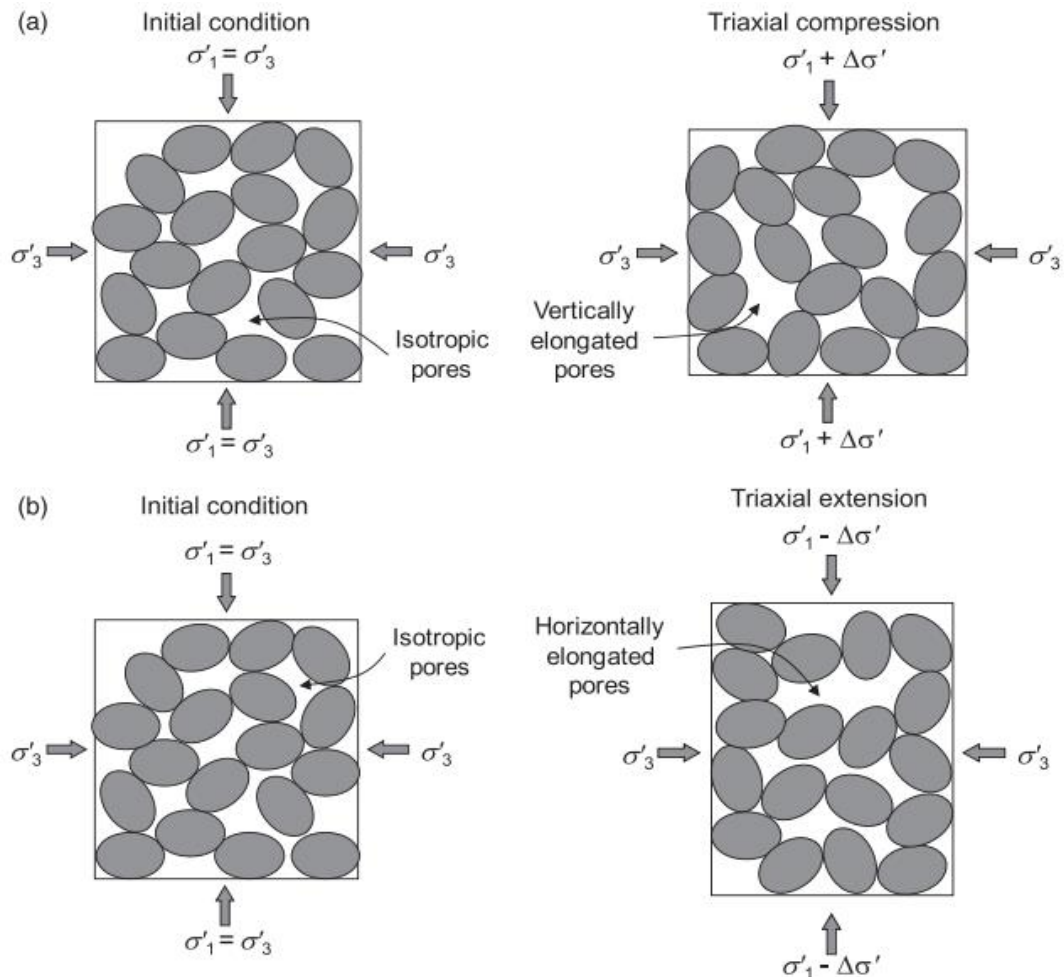


Fig. 2-3 The evolution of pore structure under (a) Triaxial compression; and (b) Triaxial extension (Chang and Zhang, 2012)

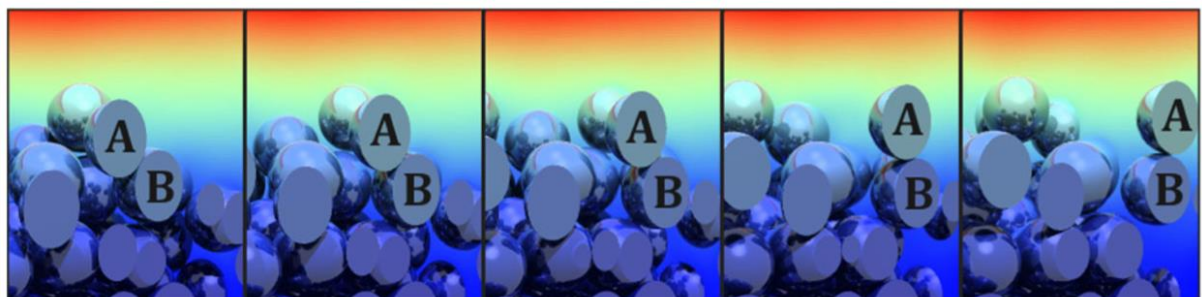


Fig. 2-4 The rotating particles, shown in time sequence from left to right (Brumby *et al.*, 2015)

The critical flow speed to trigger contact erosion was also studied through a numerical simulation (Harshani, 2017). The numerical model is illustrated with Fig. 2-5 (a). The initiation of contact erosion was recognized when the fine particles started to dislodge, and the initiating pore flow speed was the mean flow speed in the pore throat at this moment. The parameters in the numerical simulation are illustrated with Fig. 2-5 (b). Two geometrical factors that can

potentially influence the contact erosion initiation were studied: sizes of coarse particles (D_f) and widths of pores (L_p). The size of fine particles (D_b) was kept constant. The initiating flow speed was converted into the dimensionless Froude number (Fr) to allow comparison between different geometrical conditions. The Froude number was defined as:

$$Fr = \frac{u_f}{\sqrt{(S - 1)gD_b}} \quad (2-2)$$

where u_f is the mean flow speed at the pore throat detected inside a single pore when contact erosion was triggered, S and D_b are the specific gravity and diameter of fine particles respectively, and g is the gravitational acceleration.

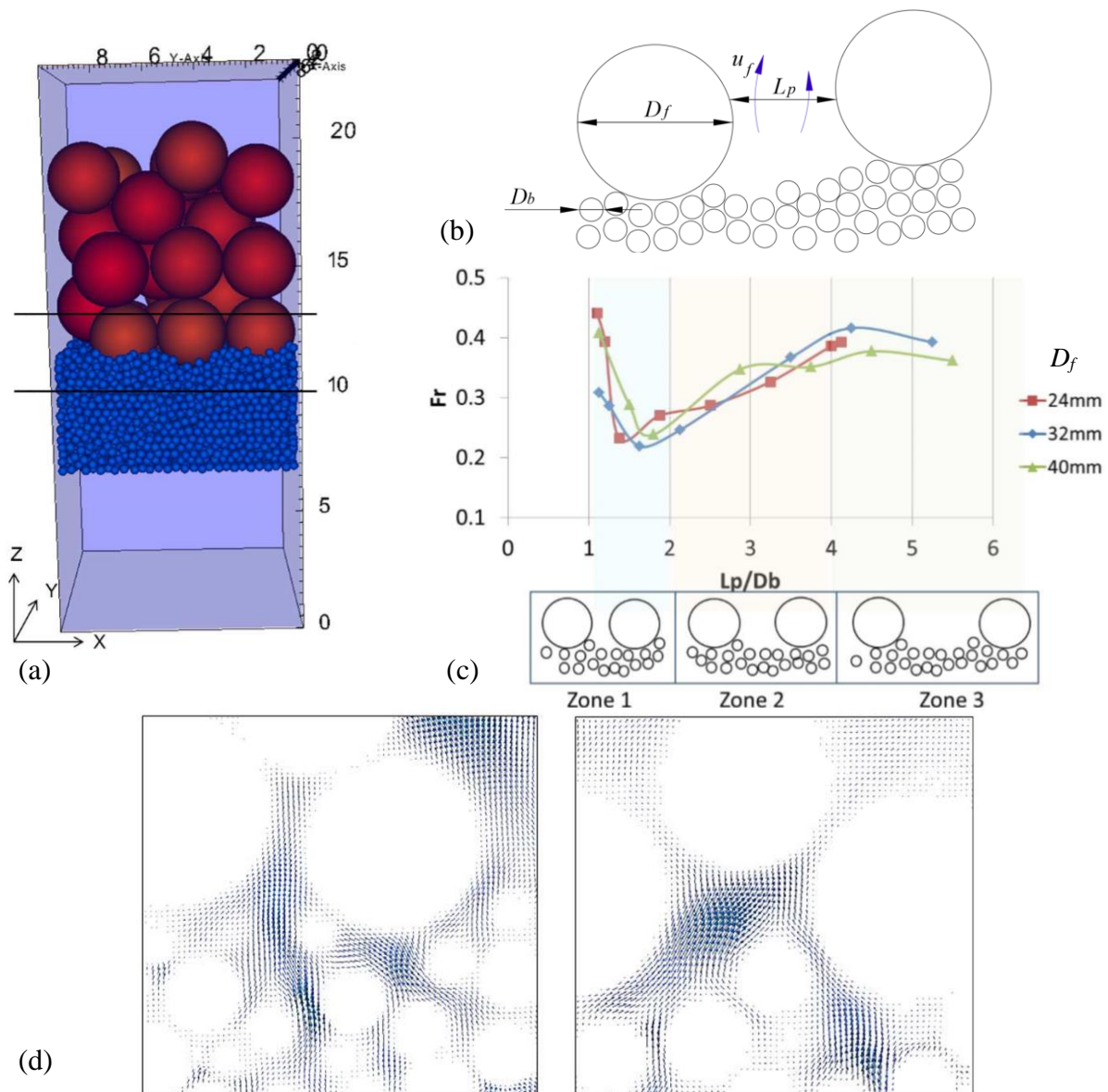


Fig. 2-5 (a) Numerical model for simulating contact erosion initiation; (b) Definition of parameters; (c) Initiating flow speed normalized with the Froude number versus L_p / D_b ; (d) Jet-like flow pattern at the top of the fine particle bed (Harshani, 2017)

The tendency of this variation is shown with Fig. 2-5 (c). The critical u_f was found to vary with L_p / D_b . Three zones of L_p / D_b were identified accordingly to describe the tendency. In Zone 1,

the initiating flow speed decreased sharply as the restriction posed by the narrow pore throat reduced. In addition, a jet-like flow pattern occurred at the top of the fine particle bed, which accelerated the dislodgement of fine particles, as shown in Fig. 2-5 (d). In Zone 2, the initiating flow speed increased, as the accelerating effect of the jet-like flow pattern diminished. In Zone 3, the geometrical condition's influence was minor, and therefore the initiating flow speed remained constant even if the geometrical condition continued changing.

A micro-scale experimental study was also conducted to investigate the initiation of contact erosion. Beguin, Philippe and Faure (2012) simulated soil particles of different sizes in contact erosion with sand and borosilicate beads, as shown in Fig. 2-6. Contact erosion was triggered by applying an external flow. The study measured the pore velocity and hydraulic shear stress in local areas at the interface between sand and borosilicate beads during the contact erosion process. The micro-scale pore velocity was measured with the particle image velocimetry (PIV) technique. The hydraulic shear stress τ was calculated with:

$$\tau = \mu \frac{\partial u_x}{\partial z} \quad (2-3)$$

where μ is the dynamic viscosity, $\partial u_x / \partial z$ is the horizontal velocity component gradient along the z -axis.

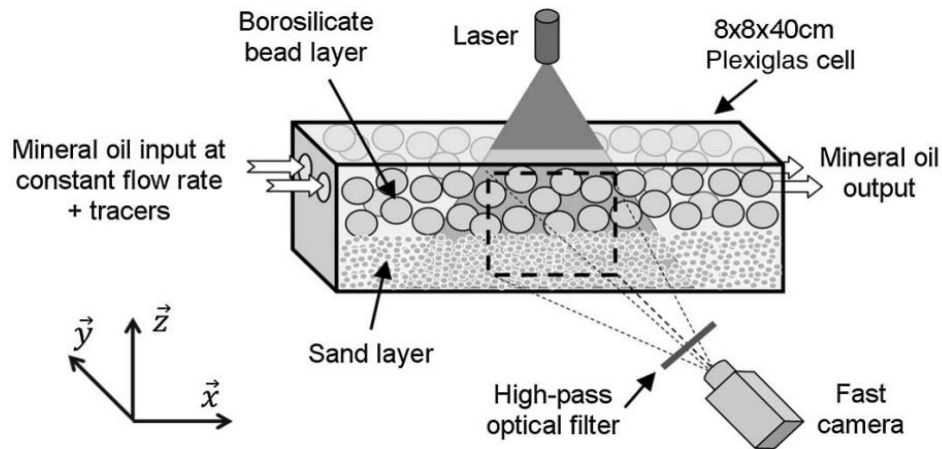


Fig. 2-6 Experimental setup for a micro-scale study on contact erosion (Beguin, Philippe and Faure, 2012)

The experimental results revealed that even when the applied flow rate was low, the pore velocity and the hydraulic shear stress can be high in some local areas at the interface between the two layers of particles. As the local velocity and hydraulic shear stress were delicate, this experiment indicated the importance to study contact erosion initiation at a micro scale.

2.1.4 Flows in granular media

As introduced in 2.1.2 and 2.1.3, the studies on contact erosion usually involved interactions between flows and granular media formed by packs of spheres. To characterize the velocity

field of micro-scale flow in granular media, the probability density function (PDF) curves were adopted in many research works. The y -coordinate of a dot on a PDF curve represents the probability of a velocity to occur in the velocity field, and the x -coordinate represents this velocity. General features for the PDF curves plotted for velocity in the flow-wise direction were: a peak at around $x = 0$, a sharp decay to the left side of the peak, and a gradual decay to the right side of the peak (Rong, Dong and Yu, 2013). The more delicate features of the curves, such as the slope of decays, were found to be influenced by the Reynolds number (a dimensionless quantity that is positively related to the flow velocity) (Rong, Dong and Yu, 2013; Abdelhamid and El Shamy, 2014) and the porosity of granular media (Rong, Dong and Yu, 2013). The decay is prolonged at a higher Reynolds number (Rong, Dong and Yu, 2013).

The flow behaviors in granular media and those in an open space are different. Two manifestations of this difference are particularly concerned in the current study on contact erosion, and are elaborated as follows.

Firstly, the drag force is exerted to an object when subjected to a viscous flow (Souza, Girardi and de Oliveira, 2017). The drag force is influenced by many factors, including roughness of the object's surface (Achenbach, 1974), the relative velocity of the viscous flow to the object, and the geometry of the object, etc. (Brown and Lawler, 2003). When granular media formed by packs of spheres are subjected to a viscous flow, the drag force is exerted to spheres. Vortices will occur on the back side of the sphere due to the drag force, as shown in Fig. 2-7. Such vortices are referred to as wakes. As the Reynolds number increases, the vortex ring of wakes becomes elongated in the flow-wise direction, and eventually becomes oscillated and turbulent (Taneda, 1956). This variation in wakes caused by the increasing Reynolds number contributes to the variation in flow velocity PDFs at different Reynolds numbers, as discussed previously.

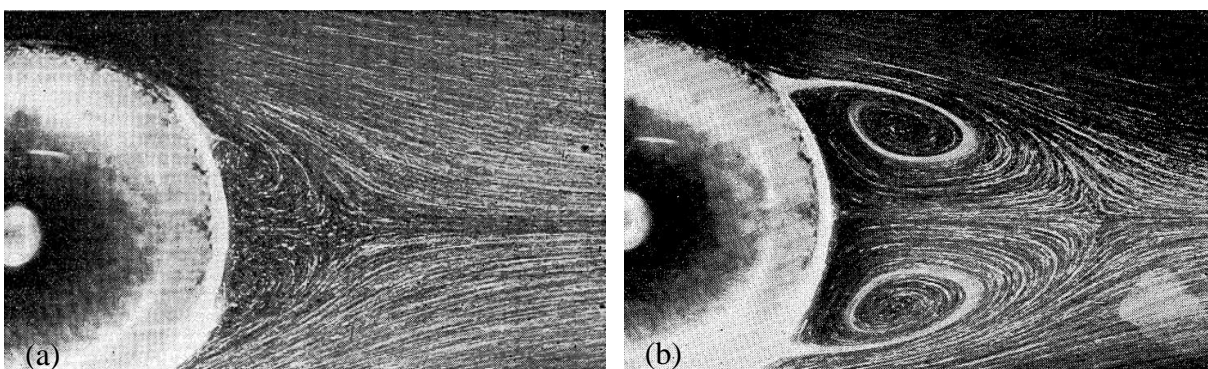


Fig. 2-7 Vortices at the back side of a sphere confronted with viscous flow, when (a) $Re = 37.7$; and (b) $Re = 73.6$ (Taneda, 1956)

Secondly, the critical Reynolds number for flows in granular media to trigger the laminar-turbulent transition was identified to be lower than that for flows in an open space. When reaching a critical Reynolds number, a smooth and steady (laminar) flow will become turbulent

and unsteady. This critical Reynolds number was measured to be around 2300 for a pipe flow without granular media (Falkovich, 2011); while the critical Reynolds number was measured to be ranged from 90 to 300 for flows in granular media. The experiments measuring the latter critical Reynolds number were conducted with granular media formed by cylinder arrangements (Dybbs and Edwards, 1984), packs of spheres of different sizes (Wegner, Karabelas and Hanratty, 1971; Jolls and Hanratty, 1966; Latifi *et al*, 1989; Rode *et al*, 1994), and Ceramic foams (Hall and Hiatt, 1996) etc. A reason for the laminar-turbulent transition to begin at a lower Reynolds number is the drag force exerted to granular media (Holdich, 2002). Thus, those factors influencing the drag force also influence this decrease in the critical Reynolds number.

2.2 Particle image velocimetry (PIV) technique

Enhanced with the PIV technique, accurate velocity data can be obtained in a spatial range simultaneously (Adrian, 1991; Grant, 1997). With this property, the PIV technique can be used for validating computational fluid dynamics (CFD) models (Grant, 1997). Once an experimental configuration consistent with a numerical model is built, flow velocity data can be obtained with the PIV technique to compare with the relevant numerical results. Many researchers observed micro-scale flows in granular media with the PIV technique. The experimental results showed good agreement with relevant numerical results (Beguin, Philippe and Faure, 2012; Moroni and Cushman, 2001; Meinicke *et al*, 2017; Yang *et al*, 2013; Johns *et al*, 2000).

2.2.1 Tracer particles

In applications of the PIV technique, a camera acquires images of the interested areas successively. The flow velocity is visualized to the camera by embedding tracer particles into the fluid. By detecting tracers' displacement in the acquired images, the flow velocity can be calculated. Thus, the tracers must track the fluid's motion strictly to obtain accurate velocity information. This means that tracers must be consistent with the fluid in density (Melling, 1997), and small enough to follow the fluid's motions. Meanwhile, tracers must be big enough and reflective to be observed in images (Raffel *et al*, 2018). In addition, the tracers were preferably to be stable inert chemicals that are not toxic, corrosive, or abrasive (Melling, 1997).

In previous studies on micro-scale flow enhanced with the PIV technique, widely-used tracer particles for liquid flows were hollow glass spheres, Aluminum flakes (Raffel *et al*, 2018), and metal oxidants (Melling, 1997) etc. Nevertheless, these tracer particles are abrasive and therefore can damage the experimental apparatus. Also, densities of these materials are much

higher than water, leading to uncertainty in tracking the flow.

In contrast, inert micron-size polymer tracers can trace water flows accurately, and is highly reflective (Sankar, Kamemoto and Bachalo, 1992). The density of polymer tracers is also similar with water, ranging from 1.03 to 1.05 kg/m³ (Melling, 1997). Hence, using micron-size polymers as tracing particles is suitable for PIV measurements conducted with water.

2.2.2 Light source

A pulsed illumination functions as the light source for the camera to acquire images in PIV measurements. One image is acquired by the camera for each time of illumination. One pair of successive images is acquired with a known time interval between twice illuminations. This time interval is referred to as the pulse distance. In image processing, the displacement of each detected particle between the two successive images is measured. The velocity data is calculated with the displacements of all detected particles and the known pulse distance (Raffel *et al*, 2018).

To obtain reliable and accurate velocity data, the pulse distance must be calibrated with the applied flow rate to ensure that valid and appropriate displacements take place during the pulse distance (Gori, Petracchi and Angelino, 2013; Fischer, Sauvage and Roehle, 2008). In other words, when a relatively low flow rate is applied, a longer pulse distance is to be adopted to ensure that adequate displacements take place; and vice versa, when a relatively high flow rate is applied, a shorter pulsed distance is to be adopted to ensure that displacements do not exceed the measuring range.

Traditionally, pulsed laser was adopted as the light source for PIV measurements (Peurrung, Rashidi and Kulp, 1995; Meinicke *et al*, 2017; Cenedese and Viotti, 1996; Patil and Liburdy, 2013). However, laser systems were energy-consuming. The whole volume of the testing section needed to be illuminated due to the difficulty in adjusting micron-size laser sheets (Akselli, Kholmatov and Nasibov, 2009). Nevertheless, the capacity was not fully utilized, as the camera can only acquire images of one single plane in the whole volume at a time (Hagsäter *et al*, 2008).

Comparing with the traditional laser-based light source, the high-power light-emitting diode (LED) light source was proven to be inexpensive and energy-efficient (Willert *et al*, 2010; Hagsäter *et al*, 2008), as well as easier to operate (Buchmann, Willert and Soria, 2012; Hagsäter *et al*, 2008). In addition, LED-based light source required minimal pre-trigger time: less than 100 ns, comparing with 100 to 300 μ s for pulsed laser (Willert *et al*, 2010). For a light source, the pulse distance cannot be shorter than its pre-trigger time. Thus, the minimum pulse distance that can be reached by a LED-based light source is 1000 times shorter than that by a laser-based

light source. As discussed previously, the pulse distance must be adjusted to be calibrated with the applied flow rate. A LED-based light source is therefore especially suitable for PIV measurements when a high flow rate is applied.

2.2.3 *Refractive index matching (RIM) methods*

The PIV technique was usually used for observing multi-phase systems. The refraction that happens when light passing through different phases in the system can lead to false displacements and unwanted distortions in the acquired images, and can cause errors in PIV measurements (Budwig, 1994). Thus, it is important for the materials in different phases to match in the refractive index.

Commonly-used solid-phase materials in PIV measurements were glass, plastics, and silicon elastomer. To match the liquids' refractive indices with those solid-phase materials, researchers tuned different aqueous solutions or organic liquids to attain wanted refractive indices. However, it was difficult to achieve perfect RIM with this method, as the proportion of different compositions of the liquid mixtures must be precisely manipulated (Budwig, 1994; Wiederseiner *et al*, 2011). In addition, some of the liquids were poisonous, or unsafe to work with, or can dissolve some components of the experimental apparatus (Budwig, 1994). The refractive indices of the liquid mixtures were also found to be unstable due to external factors, such as temperature and humidity etc. (Wiederseiner *et al*, 2011).

In contrast, using water-based hydro-gel beads and water to form the two-phase system can easily achieve RIM. Dry hydro-gel beads can absorb water equivalent to 200 times of its own weight (Lo *et al*, 2009). Due to this high water content, water-based hydro-gel beads matched with water in refractive index (Lo *et al*, 2009; Byron and Variano, 2013; Weitzman *et al*, 2014). Fig. 2-8 (a) and (b) illustrates this good match of refractive index. Hydro-gel beads were also cheap, and similar with natural soil in hydraulic characteristics (Lo *et al*, 2009). In addition, as water was adopted as the liquid-phase material, the shortcomings with the aqueous solutions or organic liquids mixtures were avoided. Thus, hydro-gel beads are ideal for PIV measurements.

2.2.4 *Image processing*

In image processing, the whole image frame is firstly divided into numerous interrogation windows (IWs). Within one IW, the displacements between two successive images of all detected tracer particles are assumed to be homogenous. The mean displacement of the detected tracer particles inside the IW features the displacement of this IW. With the known pulse distance introduced in 2.2.2, the velocity vector of this IW can be calculated. The combination of the velocity vectors of all IWs in an image frame assembles the full velocity vector field

(Harshani *et al*, 2016).

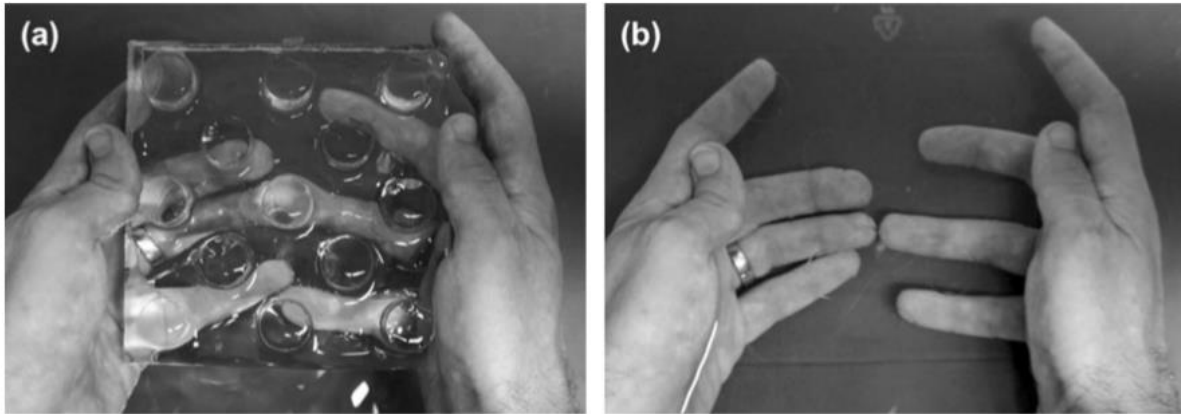


Fig. 2-8 (a) Hydro-gel beads suspended in air; and (b) Hydro-gel beads submerged in water (Weitzman *et al*, 2014)

2.3 Expansion effect

2.3.1 Significance

The expansion effect refers to the disturbance in the flow regime that occurs when a pipe flow travels through a sudden-expanding cross-section (Back and Roschke, 1972). The disturbance manifests as vortices and reverse streamlines against the applied flow (Back and Roschke, 1972), as shown in Fig. 2-9.

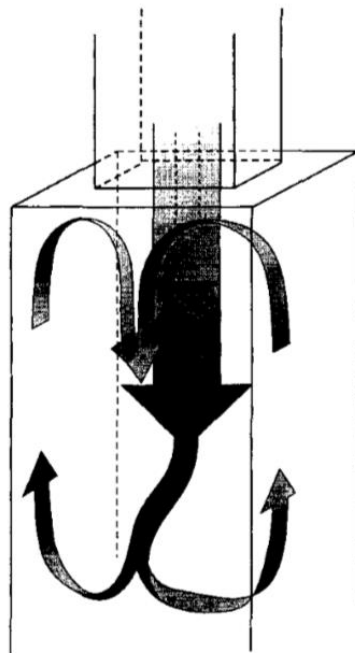


Fig. 2-9 Reverse streamlines and vortices caused by the expansion effect (Hertzberg and Ho, 1995)

The expansion effect was widely encountered in various engineering applications, such as nozzles in engines (He *et al*, 2013), and reaction chambers in catalytic reactors (Salomons *et al*, 2004), etc. Taking the reaction chamber as an example, the vortices and reverse flows caused by the expansion effect can lead to unexpected heat transfer, pressure distribution, and contaminant accumulation in the chamber. Consequently, the physical configuration of the

chamber can deform and become no longer secure. Hence, it is important to mitigate the disturbance caused by the expansion effect.

2.3.2 Flow characterization in expansion effect

Previous researchers adopted various methods to characterize the disturbance in flow regimes influenced by the expansion effect. Schematic sketching of flow regimes was used for characterizing the size and distribution of vortices (Chen *et al*, 2008; Stieglmeier *et al*, 1989; Drikakis, 1997). Velocity profiles were used for characterizing velocity distribution within a plane (Fearn, Mullin and Cliffe, 1990; Durst, Pereira and Tropea, 1993; Chiang, Sheu and Wang, 2000).

However, schematic characterizations cannot quantitatively characterize disturbance in the flow regime. Dimensionless parameters were also defined. The reverse flow speed ratio, α , was used to characterize the reverse flow in opposite direction to the applied flow, defined as (Back and Roschke, 1972):

$$\alpha = \frac{\sum v_r}{v_0} \quad (2-4)$$

where v_r is the longitudinal (flow-wise) component for reverse velocity vectors, v_0 is the applied flow velocity. When no reverse flow exists, $v_r = 0$, therefore $\alpha = 0$; the further α deviates from 0, the more disturbed the flow regime is. This dimensionless parameter α was compared versus different upstream Reynolds numbers to study flow regimes at different applied flow rates. The upstream Reynolds number is defined as the Reynolds number before the flow experiences the sudden expansion, defined as:

$$Re_0 = \frac{\rho v_0 D_0}{\mu} \quad (2-5)$$

where ρ and μ are the density and dynamic viscosity of the fluid respectively, D_0 is the geometric dimension of the experimental configuration before the sudden expansion, typically the diameter or width of the inlet pipe.

Another dimensionless parameter, tortuosity, was defined to characterize vortices. Tortuosity was defined as (Aminpour *et al*, 2018; Duda, Koza and Matyka, 2011; Saomoto and Katagiri, 2015; Jin *et al*, 2015):

$$T = \frac{\sum u}{\sum v_y} \quad (2-6)$$

where u is the magnitude of each velocity vector in the vector field, and v_y is the longitudinal component of each velocity vector, with the direction of the applied flow defined as positive.

When no vortex exists, velocity vectors are all in the direction of the applied flow and no perpendicular component exists, thus $\Sigma u = \Sigma v_y$, and $T = 1$; the further T deviates from 1, the more or larger the vortices are.

2.3.3 Expansion effect mitigation

Attempts were made to mitigate the disturbance caused by the expansion effect. Experiments showed that the disturbed flow regime was stabilized as the flow developed along the longitudinal direction (Stieglmeier *et al*, 1989). The degree of disturbance was related to the geometrical configuration of the expanding section (Drikakis, 1997; Back and Roschke, 1972; Roy, Majumder and Sanyal, 2010; Stieglmeier *et al*, 1989) and the Reynolds number (Re) (Hammad, Ötügen and Arik, 1999; Back and Roschke, 1972; Roy, Majumder and Sanyal, 2010). These two influencing factors intersect with each other. For example, the expansion ratio was used for characterizing the geometrical configuration of the expanding section, defined as the ratio between the dimensions (typically width or diameter) of the cross-section before and after the expansion. When the expansion ratio was 1:1.2, numerical results showed that the disturbance was stabilized as Re increased (Roy, Majumder and Sanyal, 2010); in contrast, when the expansion ratio was 1:2, the disturbance became severer as Re increased, manifested as more (Drikakis, 1997) or larger (Chen *et al*, 2008) vortices. Thus, different Re s' impact on flow regimes influenced by the expansion effect can vary for different geometrical configurations.

Numerical studies also predicted that the disturbance caused by the expansion effect can be stabilized by placing porous screens at the expanding plane. The stabilizing effect was more effective as the thickness of the screen increased or the permeability (ability to allow fluids to pass through) decreased (Chen *et al*, 2008; Assato, Pedras and De Lemos, 2005). However, these numerical simulations regarding the permeability of porous screens focused only on high Re conditions, with a minimum Re of 800. The knowledge about how permeability of the porous screen influences the expansion effect at low Re is still limited.

3 Scope of Project

3.1 Statement of problems

The critical pore flow speed to trigger contact erosion will be investigated experimentally at a micro scale. The variation in the critical pore flow speed caused by different geometrical arrangements of particles will be studied. To allow comparison with numerical results, the experimental setup will be conformed to the previous numerical simulation conducted by Harshani (2017). A uniform flow is needed to be applied to the testing section as the boundary

condition to keep consistent with the numerical simulation. A uniform flow is defined as being in the same longitudinal direction, and constant along the perpendicular direction.

Nevertheless, the applied flow will travel through a sudden-expanding cross-section before entering the testing section, due to the geometrical configuration of the testing chamber used in the experiment. The flow will therefore experience the expansion effect and become disturbed. To attain the wanted boundary condition, a secondary yet prior task will be to stabilize the disturbance in the flow regime.

3.2 Objectives

Methods to stabilize the disturbance are available in previous research works, as introduced in 2.3.3. Under the context of the current project, the objectives in studying the expansion effect are:

- To find out how the disturbance caused by the expansion effect changes at different flow rates (Reynolds numbers);
- To find out how the disturbance caused by the expansion effect changes when porous screens are placed at the expanding plane, and how this change relates to the permeability of screens;
- To find out how the disturbance caused by the expansion effect changes when a granular medium is placed along the flow path, and how different flow rates (Reynolds numbers) and porous screens influence this change;

The variation in the critical pore flow speed (u_f) to trigger contact erosion caused by different geometrical conditions will be tested. When the expected boundary condition is attained, the objectives in investigating u_f are:

- To find out how u_f changes with different size ratios between pore widths and fine particle diameters;
- To find out how u_f changes with different size ratios between fine and coarse particle diameters.

4 Methodology

4.1 Experimental setup

4.1.1 Water circulation system and testing section

The experimental setup is illustrated with Fig. 4-1 (a) and (b). A double-layer cylinder bucket is placed on a shelf. Water is constantly pumped from the reservoir through a pipe into the inner

cylinder bucket to form and maintain a 2-m-high water head. As water being constantly pumped into the inner cylinder bucket, water overflows into the outer cylinder bucket, and is directed back to the reservoir. The inner cylinder is connected to the bottom of the testing chamber with a pipe to provide a pressure-driven waterflow. The flow rate of this waterflow is measured with a digital flowmeter, and can be adjusted with a valve. After travelling through the testing chamber, the waterflow is directed back to the reservoir through a pipe from the top of the chamber. A water circulation system is then formed.

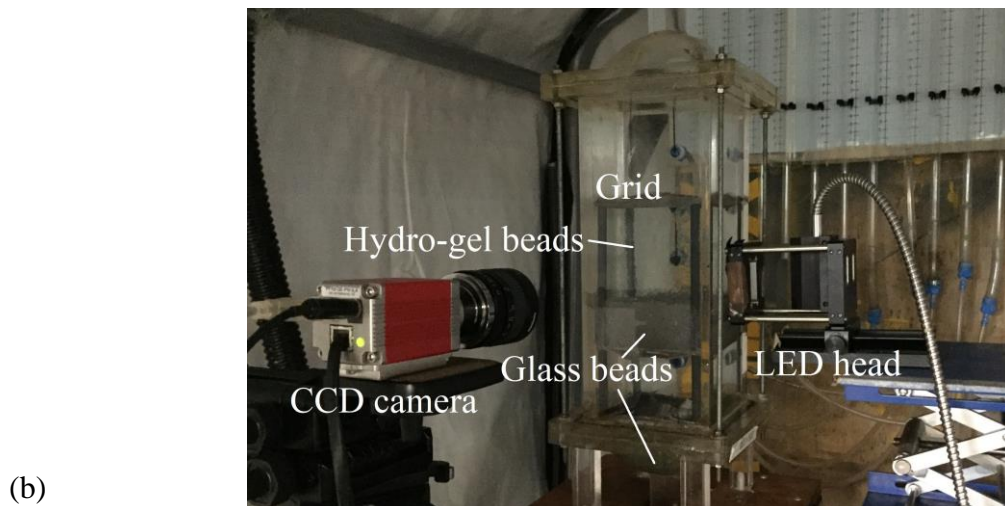
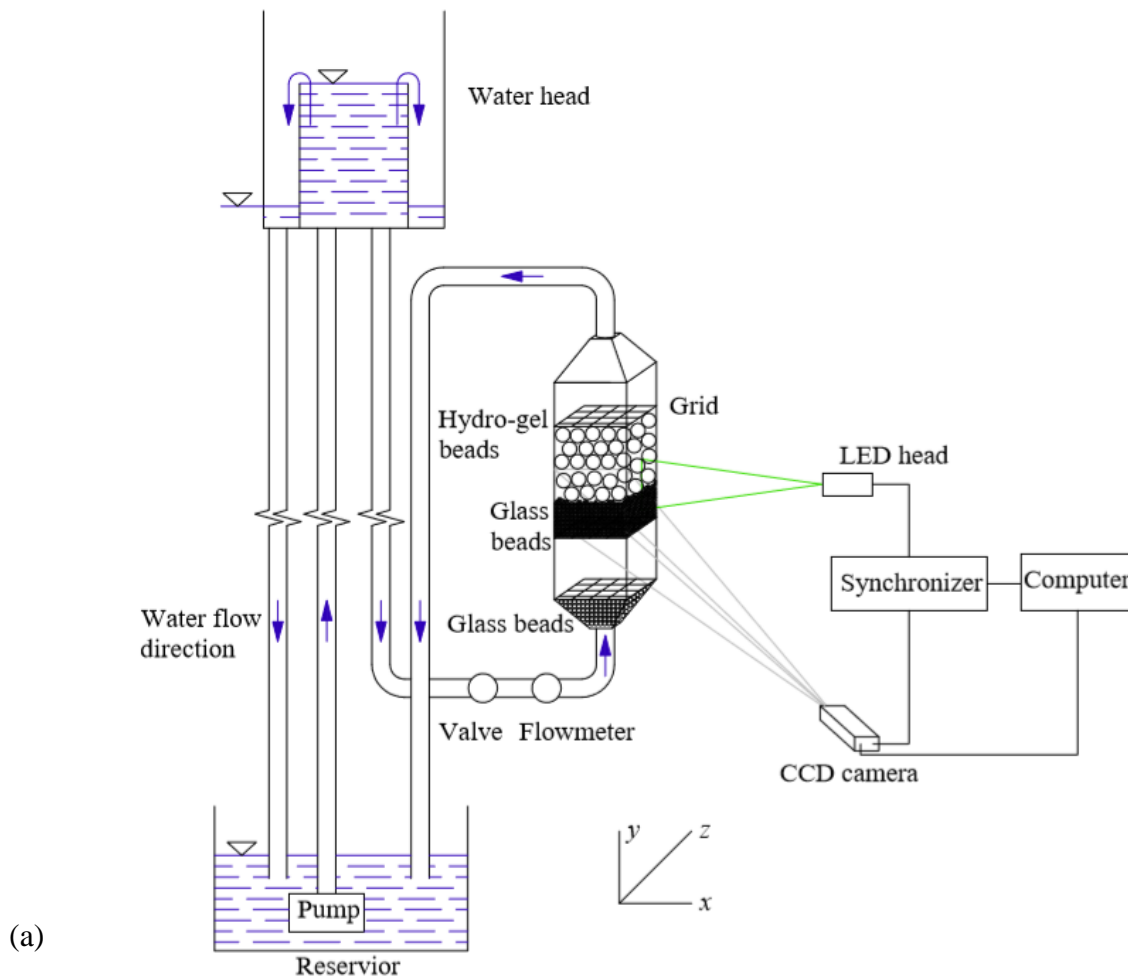


Fig. 4-1 (a) Schematic drawing; and (b) Photograph of the experimental setup

The testing chamber is functioned with a $10 \times 10 \times 30 \text{ cm}^3$ ($W \times L \times H$) square chamber with full optical access. Two 5-cm-high conical funnel openings are at both ends of the chamber, connected to the pipes with an external diameter of 3.5 cm, as shown in Fig. 4-2. The xyz -coordinate is shown in Fig. 4-1 and Fig. 4-2. The y -axis represents the longitudinal direction, with the direction of the applied flow defined as positive.

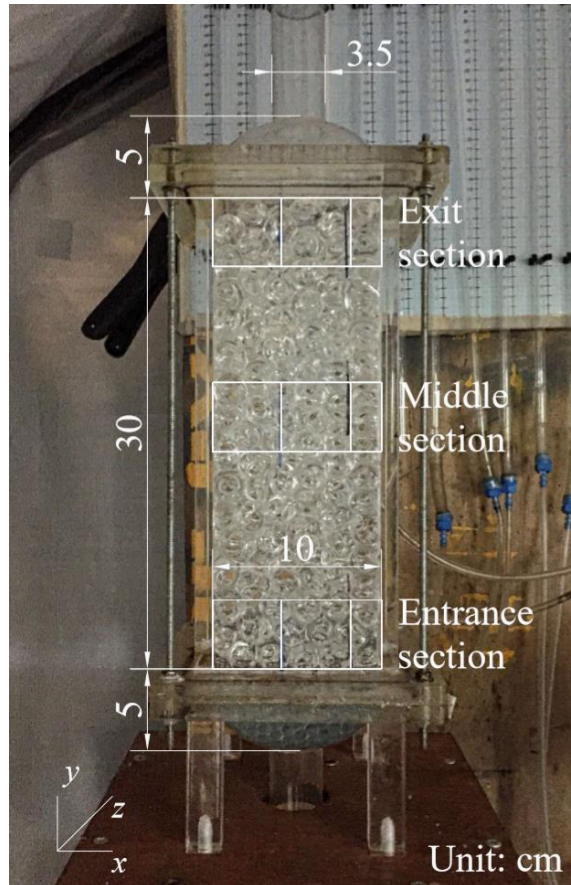


Fig. 4-2 Testing section dimensions and division, filled with hydro-gel beads

4.1.2 PIV system

The PIV technique has been adopted and validated in many research works in investigating the micro-scale flow in granular media, as introduced in 2.2. A PIV system is used in this project for micro-scale velocity measurements of the waterflow inside the chamber.

The hardware equipment acquires images of waterflow, and the images are analyzed with software to obtain velocity data. The hardware equipment in the PIV system is shown in Fig. 4-1 (a) and (b). The PIV equipment applied in this project consists of a digital charge-coupled device (CCD) camera, a LED head, a computer and a synchronizer. The LED head can be moved along the z -axis, and illuminates areas in the xy -plane. The CCD camera can be moved in the xy -plane. The images are acquired by the CCD camera in the illuminated areas. Images of different xy -planes along the z -axis can be acquired by moving the LED head along the z -axis. The timing and pulse distance for the LED head to fire are controlled by the synchronizer,

and adjusted with the computer. The synchronizer also synchronizes the working time pace of the CCD camera with that of the LED head.

RIM between the solid- and liquid-phase materials is achieved with water-based hydro-gel beads and water. Fig. 4-2 shows the hydro-gel beads suspended in air, and Fig. 4-1 (b) shows hydro-gel beads submerged in water. As hydro-gel beads become transparent in water, RIM is achieved. Water used in the water circulation system of the experimental setup is seeded with 20- μm -diameter polyamide seeding particles (PSPs) as tracers.

The acquired images are processed with the PIVView 2C software to obtain velocity data. In detecting micro-scale flow in a granular medium, this experiment focuses on motions of the flow. The granular medium is fixed with grids, as shown in Fig. 4-1 (b). In the acquired images, where IWs (introduced in 2.2.4) are located on the hydro-gel beads, the detected particles commit no displacement, or only minor displacements due to rotation of hydro-gel beads (introduced in 2.1.3). In other words, the velocity vectors located in the hydro-gel beads' regions are not indicating velocity information of the flow, and are therefore not concerned. To avoid the bias caused by these unconcerned velocity vectors in data analysis of the flow velocity, these vectors need to be excluded. Thus, those regions are hidden by applying an image mask in image processing with the PIVView 2C software to exclude these vectors.

The flow velocity data is further processed with MATLAB. The methods to characterize micro-scale flows in previous research works are adopted, including PDFs and the dimensionless parameters.

4.2 Experimental procedure

4.2.1 Experiments for expansion effect

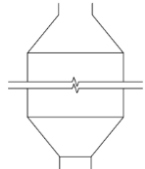
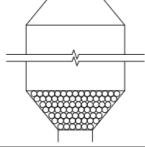
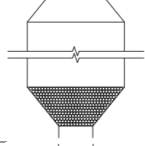
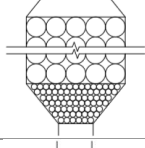
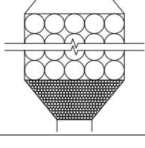
The aim of studying the expansion effect in this project is to stabilize the disturbance in the testing chamber. As discussed in 2.3.3, the disturbance is influenced by the Reynolds number (Hammad, Ötügen and Arik, 1999; Back and Roschke, 1972), the geometrical configuration of the expanding section (Drikakis, 1997; Back and Roschke, 1972; Roy, Majumder and Sanyal, 2010; Stieglmeier *et al*, 1989), and the thickness and permeability of the porous screen placed at the expanding plane (Chen *et al*, 2008; Assato, Pedras and De Lemos, 2005). The physical configuration of the testing chamber used in this experiment can hardly be modified. Thus, this study on the expansion effect focuses on how different Reynolds numbers and porous screens influence the disturbance. The porous screens are placed in the conical funnel opening at the bottom of the chamber, where waterflows travel into the chamber and experience the expansion.

As introduced in 2.1.4, studies in contact erosion usually involved interactions between flows

and granular media formed by packs of spheres. Thus, the flow regime influenced by the expansion effect in a granular medium is also investigated in this part of study. A pack of 1.8-cm-diameter hydro-gel beads is placed in the chamber to form a granular medium. The impact of different Reynolds numbers and porous screens is also studied for flows travelling through the granular medium.

All test conditions are summarized in Table 4-1. The test conditions are categorized into five groups according to the experimental configurations.

Table 4-1 Test conditions for the micro-scale flow study

Group #	Case #	Applied flow rate (lit/min)	Screen condition	Medium condition	Schematic profile
A	A1	0.1	None	Empty chamber	
	A2	1			
	A3	2			
	A4	4			
	A5	8			
B	B1	0.1	Coarse glass beads $d = 5$ mm	Empty chamber	
	B2	1			
	B3	2			
	B4	4			
	B5	8			
C	C1	0.1	Fine glass beads $d = 1$ mm	Empty chamber	
	C2	1			
	C3	2			
	C4	4			
	C5	5			
D	D1	0.1	Coarse glass beads $d = 5$ mm	Granular medium $d = 1.8$ cm	
	D2	1			
	D3	2			
	D4	4			
	D5	8			
E	E1	0.1	Fine glass beads $d = 1$ mm	Granular medium $d = 1.8$ cm	
	E2	1			
	E3	2			
	E4	4			
	E5	5			

Three different conditions for porous screen are tested with an empty chamber: no screen, 5-mm-diameter coarse glass beads screen, and 1-mm-diameter fine glass beads screen, for Group A, B and C respectively, as shown in Fig. 4-3. With smaller glass beads, the permeability of the fine glass beads screen is lower (Shepherd, 1989). The contrast between Group A and Group B, C aims at studying the effectiveness of porous screens in stabilizing the disturbance caused by the expansion effect. The contrast between Group B and Group C aims at studying how permeability of the porous screen influences the stabilizing effect.

Another two groups of tests are conducted when the chamber is filled with the granular medium.

The screen conditions are the coarse glass beads screen and the fine glass beads screen, for Group D and E respectively. The contrast between Group D, E and Group B, C is to study how the granular medium influences the disturbance caused by the expansion effect. The porosity (the ratio between the void volume and the inner volume of the chamber in this case) of the granular medium is measured to be 0.35.

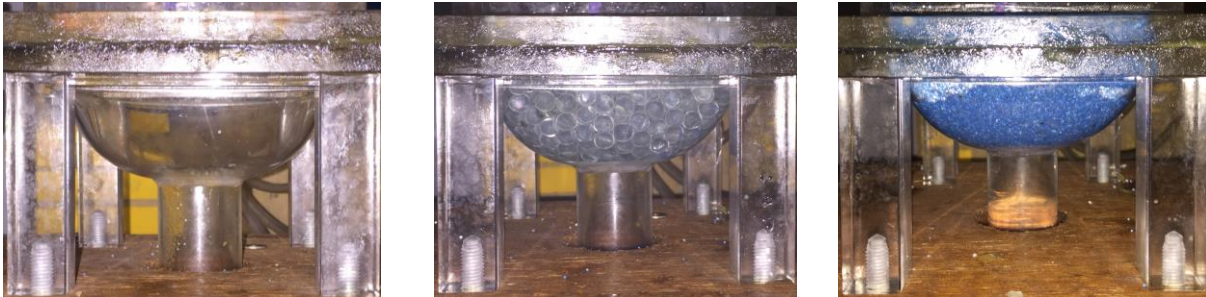


Fig. 4-3 Porous screen conditions in Group A, Group B, D, and Group C, E (a) No porous screen; (b) 5-mm-diameter coarse glass beads screen; and (c) 1-mm-diameter fine glass beads screen

Each group of tests is conducted at five different flow rates applied to the chamber to study the stabilizing effect of different Reynolds numbers. When the fine glass beads screen is placed at the bottom opening, the maximum flow rate can be reached is 5 lit/min, as the water head cannot overcome the screen's low permeability. Thus, the flow rates applied for Group A, B, and D (when no screen or the coarse glass beads screen is placed) are 0.1 lit/min, 1 lit/min, 2 lit/min, 4 lit/min and 8 lit/min; the flow rates for Group C and E (when the fine glass beads screen is placed) are 0.1 lit/min, 1 lit/min, 2 lit/min, 4 lit/min and 5 lit/min.

The flow rate is measured with a digital flowmeter (MagMaster produced by ABB Group), and is adjusted with a valve, as introduced in 4.1.1. Once the desired flow rate for one test is reached, the valve is fixed and the flow rate remains unchanged during this test. The camera is then moved around in the xy -plane to acquire images in different areas for the PIV measurement. The chamber is divided into three sections to observe representative flow regimes at different parts of the chamber, namely entrance, middle and exit. Due to the limited camera field of view (FOV), each section is divided into three windows, as shown in Fig. 4-2. Each window can be covered by one FOV. Sixteen pairs of images is acquired at each window by the camera. The camera is then moved around in the xy -plane to acquire images of other windows or other sections. After finishing acquiring images of all nine windows of the entire chamber, the flow rate is adjusted and moved on to another flow rate condition.

A detailed working methodology of the PIV technique is elaborated in 2.2 and 4.1.2. A velocity vector field is obtained for each test condition. The disturbance can be studied with velocity vector fields. By comparing velocity vector fields obtained under different test conditions, variations in the disturbance can be investigated. As discussed previously, sixteen pairs of

images are acquired for each detected area under each test condition. In image processing, the velocity vectors obtained from the sixteen pairs of images are averaged to mitigate possible bias in measuring and image processing.

4.2.2 Experiments for contact erosion initiation

The aim of this part of study is to assess how different geometrical conditions influence the critical flow speed to trigger contact erosion. As introduced in 2.1.1, contact erosion involves the contact between fine and coarse soil particles. In this study, the fine particles are referred to as the base particles, and the coarse particles are referred to as the filter particles. Base particles are placed at the bottom of the testing section, and filter particles at the top. An external flow is applied from bottom to top of the testing section to trigger contact erosion. The flow rate is constantly increased, until the base particles start to dislodge from their original layer, when contact erosion is signaled. A dislodged base particle then travel into the filter particle layer through a pore between adjacent filter particles. The initiating pore flow speed is measured as the mean velocity in this pore at the moment when the dislodgment begins.

Noticeably, tangential (horizontal) external water flow was applied to the testing section in previous research works as illustrated with Fig. 2-2 and Fig. 2-6. In those experimental setups, the applied flow was parallel to the interface between two particle layers to simulate the horizontal underground water applied to embankments and dams. Nevertheless, when a tangential flow is applied, the forces loaded on a single base particle are not in the same direction, as shown with Fig. 4-4 (a). In contrast, when a vertical flow (from bottom to top) is applied, F_D (the drag force) and F_G' (the net force of gravity, friction force and buoyancy force) are both in the vertical direction, as shown with Fig. 4-4 (b). In studying the critical pore flow speed to trigger dislodgement of a fine particle, the focus is on the critical balance of forces. Thus, a vertical external flow greatly simplifies the force addition on a single base particle, and is therefore more suitable for this study.

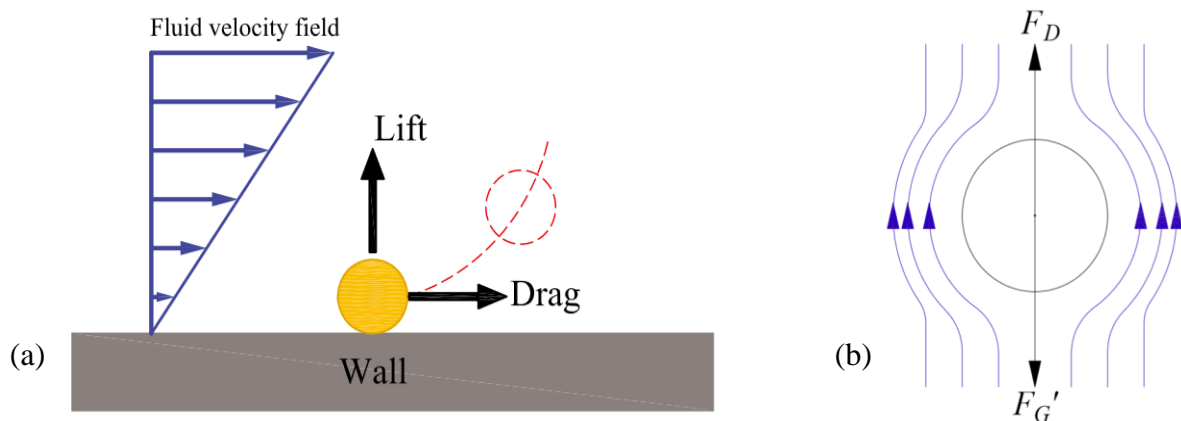


Fig. 4-4 Force analysis of a base particle when (a) A tangential flow is applied (Abdelhamid and El Shamy, 2014); and (b) A vertical flow is applied

The experimental design for learning contact erosion initiation conforms to the numerical simulation conducted by Harshani (2017). In the experiment, the filter particles are configured with hydro-gel beads to achieve RIM with water. The base particles are configured with glass beads. On the one hand, glass beads of the desired sizes can be easily obtained; on the other hand, the flow velocity in the base particle layer is not of interest in this project, and therefore RIM between base particles and water is not needed.

In the experimental setup, the base particles (smaller glass beads) are placed below the filter particles (larger hydro-gel beads) at the middle section of the chamber, as shown in Fig. 4-1. Fig. 2-5 (b) illustrates the definition of parameters. The pore throat length, the diameters of filter particles and base particles are denoted with L_p , D_f and D_b respectively. Two size ratios are introduced to describe the geometrical conditions: the size ratio between filter and base particles (D_f / D_b), and the size ratio between pore throat length and base particle diameter (L_p / D_b). The test conditions are summarized in Table 4-2.

Table 4-2 Test conditions for the contact erosion initiation study

Group #	Case #	D_f (mm)	D_b (mm)	D_f / D_b
F	F1	12	1	12:1
	F2	12	1.5	8:1
	F3	12	2	6:1
	F4	18	3	6:1

Three different (D_f / D_b)s are tested in Case F1, F2, and F3, F4 respectively. The contrast between Case F3 and Case F4 aims at testing if the absolute sizes of filter particles and base particles influence the experimental results. The size ratio in Case F4 is the same with that in Case F3, but the diameters of filter particles and base articles are both 1.5 times of those in F3.

The transitional area between the filter particle layer and the base particle layer is observed with the PIV system. The CCD camera acquires images at different spots in this transitional area. Different L_p s are observed in different spots, ranging from D_b to seven times D_b . This is repeated for all four groups of geometrical conditions as listed in Table 4-2. The micro-scale real-time motion of each spot is monitored with the PIV system. Sixteen pairs of images are acquired continuously before and after the dislodgement starts at each spot. The image processing method introduced in 4.2.1 averages the velocity vectors obtained from the sixteen pairs of images to mitigate possible bias in measuring and image processing. Different from that, the vectors in the sixteen image pairs in this experiment are not averaged. The positions of base particles are compared carefully in the sixteen pairs of images to find the image pair that is taken at the moment when the dislodgement begins. This only image pair is selected to be processed, and to obtain velocity vector field information.

Different from the experimental procedure for studying the expansion effect introduced in 4.2.1, the flow rate is not fixed in triggering contact erosion. The position of the camera is fixed when detecting each spot, and the flow rate is slowly increased, until dislodgement starts in the detected area.

As discussed in 3.1, a uniform flow must be applied to the testing section as the boundary condition to eliminate bias and to keep consistent with the numerical simulation. The experimental setup design benefits from the conclusions drawn from the first part of study: stabilization of the disturbance in flow regimes caused by the expansion effect. This optimization will be further discussed in 5.2.1. For each geometrical condition, a pre-test is conducted to ensure that a uniform flow is applied. Different applied flow rates are required for base particles of different sizes to dislodge. A flow rate similar to the required flow rate is applied to the testing chamber in the pre-tests for each geometrical condition. The flow at the boundary of the testing section is tested with the PIV system to ensure the uniformity.

5 Results and Discussion

5.1 Expansion effect: disturbance and stabilization

5.1.1 Velocity distribution in empty chamber

Velocity vector field graphs can be generated with velocity data to describe flow regimes at the observed areas. Fig. 5-1 (a) to (c) show the vector field graphs generated with velocity data obtained from tests conducted with the experimental configurations of Group A, B and C respectively. The experimental configurations are empty chamber with no porous screen, empty chamber with coarse glass beads screen, and empty chamber with fine glass beads screen, respectively. The screen conditions are illustrated in the vector field graphs with sketching. The applied flow rates are 0.1 lit/min, 1 lit/min, 2 lit/min, 4 lit/min and 8 lit/min for the five vector field graphs in Fig. 5-1 (a) and (b) from left to right, respectively. In Fig. 5-1 (c), the highest flow rate applied is 5 lit/min due to the fine glass beads screen's low permeability, as discussed in 4.2.1.

The flow is applied from bottom to top of the testing chamber, namely upwards in the vector field graphs. The upwards velocity vectors in the velocity vector field graph are featured with blue arrows; the downwards velocity vectors are featured with magenta arrows. The arrow lengths indicate velocity magnitudes, and the same length scale is applied to all the graphs. Three sections of the testing chamber are detected, as shown in Fig. 4-2. The three areas showing arrows in each velocity vector field graph in Fig. 5-1 (a) to (c) from bottom to top are

the entrance, middle and exit sections of the testing chamber respectively. The blank areas between two sections in the graphs are not detected. The height of these blank areas are not in proportion with the actual configuration.

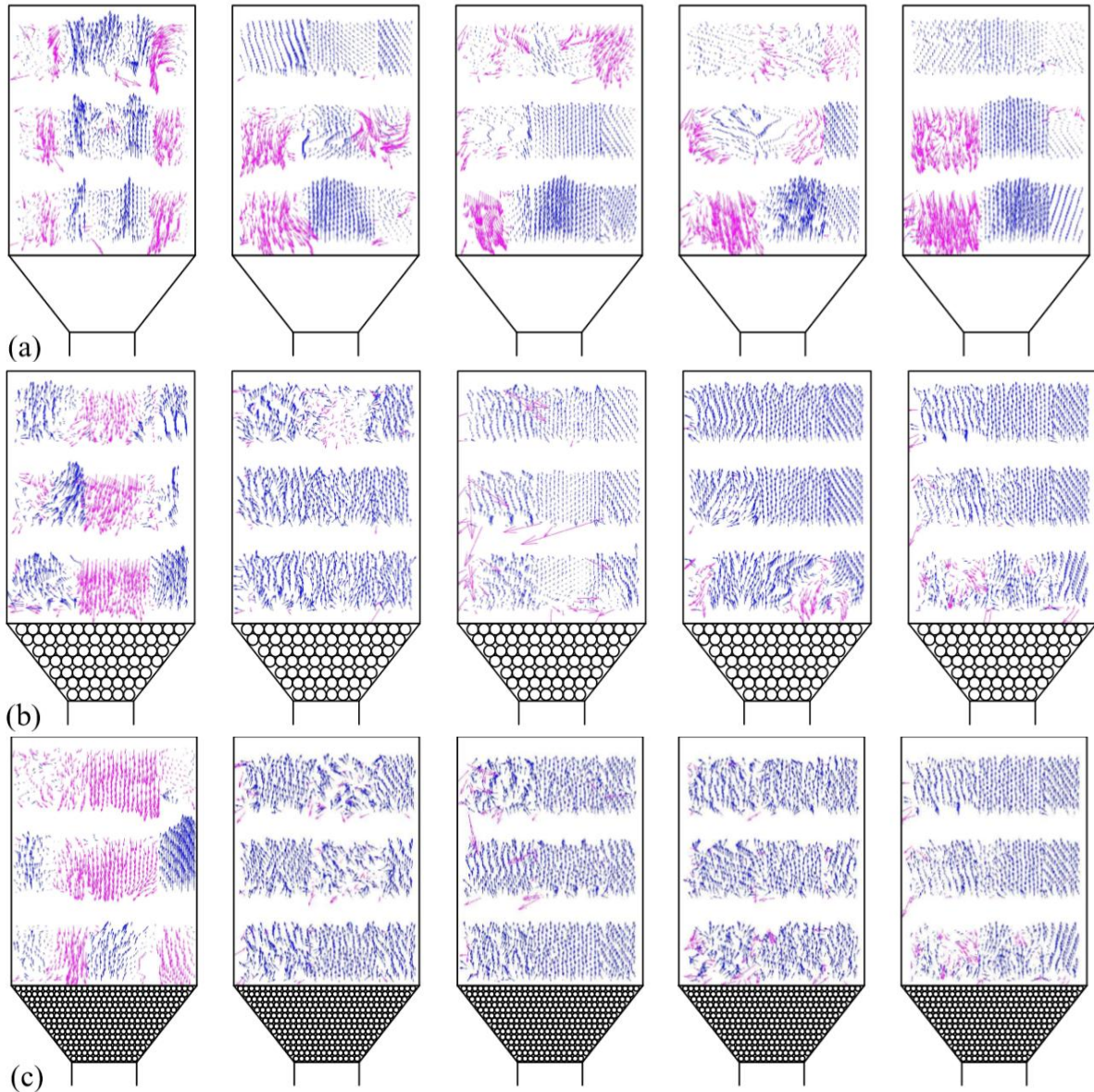


Fig. 5-1 Vector field graphs for different experimental configurations: **(a)** Group A, empty chamber with no porous screen; **(b)** Group B, empty chamber with coarse glass beads screen; and **(c)** Group C, empty chamber with fine glass beads screen. With upwards velocity plotted in blue and downwards velocity plotted in magenta. Applied flow rates from left to right: for Group A and B, 0.1 lit/min ($Re_c = 16.67$), 1 lit/min ($Re_c = 166.67$), 2 lit/min ($Re_c = 333.33$), 4 lit/min ($Re_c = 666.67$), and 8 lit/min ($Re_c = 1333.33$); for Group C, 0.1 lit/min, 1 lit/min, 2 lit/min, 4 lit/min, and 5 lit/min ($Re_c = 833.33$)

When different flow rates are applied, the overall magnitude of velocity in each graph will vary. Corresponding, the overall length of arrows in each graph will vary. This poses an obstacle in qualitative comparison between vector field graphs obtained at different applied flow rates. To eliminate this obstacle, the magnitude of each velocity vector is normalized with the mean Darcy flow speed, u_D , defined as (Harshani, 2017):

$$u_D = \frac{q}{A} \quad (5-1)$$

where q is the applied flow rate, A is the cross-sectional area of the chamber. Thus, the magnitude of each velocity vector in the vector graphs is denoted with u_g :

$$u_g = \frac{u}{u_D} \quad (5-2)$$

where u is the velocity magnitude of each detected velocity vector in the velocity vector field.

The Reynolds number is a dimensionless quantity to predict the flow pattern (Falkovich, 2011). The chamber Reynolds number, Re_c , used in this part of discussion is defined as:

$$Re_c = \frac{\rho u_D L}{\mu} \quad (5-3)$$

where L is the width of the chamber, ρ and μ are the density and dynamic viscosity of water respectively.

In Fig. 5-1 (a), when no porous screen is placed at the expanding plane, the distribution of velocity vectors do not show a specific changing pattern as the applied flow rate increases. Vortices or downwards velocity vectors are observed for all five graphs. In Fig. 5-1 (b) and (c), when porous screens are placed at the expanding plane, the downwards velocity and vortices also appear at a low applied flow rate ($q = 0.1$ lit/min). According to previous research works discussed in 2.3.1, the disturbance caused by the expansion effect manifests as vortices and reverse streamlines (Back and Roschke, 1972). The flow regimes in the tests conducted without a porous screen, and the tests conducted with a porous screen but at a low applied flow rate ($q = 0.1$ lit/min) are therefore recognized as being disturbed by the expansion effect.

In contrast, as the applied flow rate increases ($q \geq 1$ lit/min), the disturbed flow regimes in Fig. 5-1 (b) and (c) are stabilized. No vortex is seen. The velocity vectors are predominantly upwards. Thus, when a porous screen is placed at the expanding plane, the disturbance caused by the expansion effect is stabilized as the applied flow rate, or the chamber Reynolds number, increases. In contrast, this stabilizing effect is not observed when no porous screen is placed. This result matches with the conclusions drawn from previous research works, that the disturbance caused by the expansion effect can be stabilized by placing porous screens at the expanding plane (Roy, Majumder and Sanyal, 2010; Chen and Li, 2003).

To study the velocity distribution in more details, the probability density function (PDF) is introduced, as shown in Fig. 5-2. The PDF curves are generated by normalizing histograms with the number of velocity vectors detected. In other words, the x -coordinate of each dot on the curves represents a velocity; the y -coordinate is the frequency for this velocity to appear in the velocity vector field divided by the total number of detected velocity vectors. Thus, each

dot in a PDF curve indicates the probability for the corresponding velocity in x -axis to appear in the velocity vector field. Again, to allow comparison between velocity data obtained at different applied flow rates, the velocity magnitude is normalized with the mean Darcy flow speed, u_D .

The PDFs for velocity data obtained from tests conducted with experimental configurations of Group A, B and C at different applied flow rates are plotted in Fig. 5-2 (a), (b) and (c) respectively. Each curve in a PDF graph represents a test conducted at an applied flow rate. The velocity components in the flow-wise direction (v_y) are plotted. The velocity data obtained from the middle section of the chamber is used.

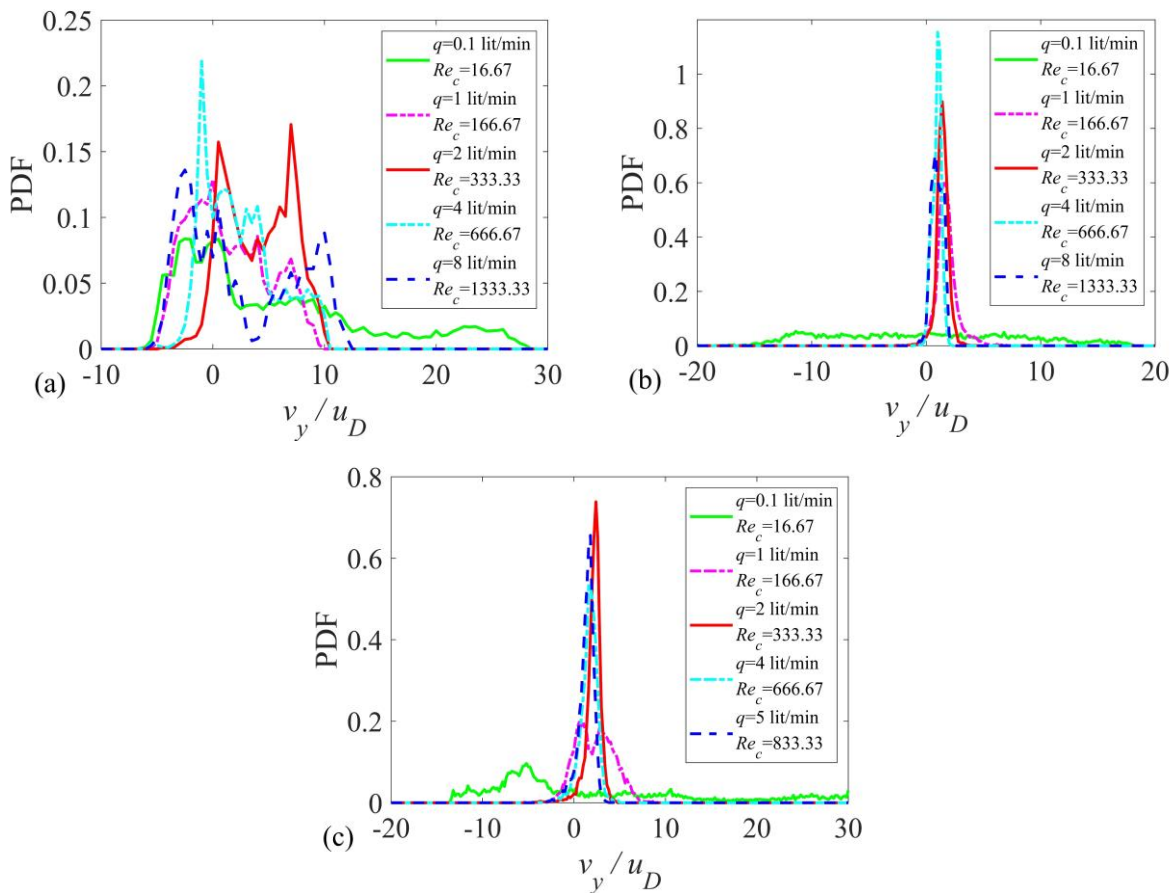


Fig. 5-2 PDF plotting of flow-wise velocity components in the middle section at different applied flow rates for (a) Group A, empty chamber with no porous screen; (b) Group B, empty chamber with coarse glass beads screen; and (c) Group C, empty chamber with fine glass beads screen

In Fig. 5-2 (a), the range of velocity probability distribution along the x -axis is relatively wide. Downwards velocity, namely negative value of v_y / u_D , exists for all curves. The curves do not show a specific pattern of change as the applied flow rate increases. The wide velocity probability distribution range and relatively high proportion of negative value in v_y / u_D are also observed in Fig. 5-2 (b) and (c) when $q = 0.1$ lit/min. As discussed previously, disturbance caused by the expansion effect occurs under these test conditions in the form of vortices and reverse streamlines against the applied flow. Thus, the PDF curves for disturbed flow regimes

are featured with a wide range of velocity probability distribution, and a relatively high proportion of negative value in v_y / u_D .

In contrast, as a porous screen is placed, the velocity probability distribution becomes more concentrated when the applied flow rate is higher than 0.1 lit/min. In Fig. 5-2 (b), A sharp increase occurs to the right of $v_y / u_D = 0$ for curves derived from tests conducted at higher applied flow rates ($q \geq 1$ lit/min). A peak occurs to the right of $v_y / u_D = 0$. The decay after this peak is more gradual for lower applied flow rates ($q = 1$ lit/min and $q = 2$ lit/min), and sharper for higher applied flow rates ($q = 4$ lit/min and $q = 8$ lit/min). This sharp decay indicates that the velocity probability distribution is more concentrated for higher applied flow rates, or higher chamber Reynolds numbers. A more concentrated velocity probability distribution means that the variation range for velocity vector magnitudes is smaller. Therefore, the flow velocity is uniform, and the disturbance is stabilized. Thus, as the disturbance caused by the expansion effect is stabilized, the PDF curves are featured with a peak to the right to $v_y / u_D = 0$, and a concentrated velocity probability distribution.

The following conclusions can be drawn from the differences between Fig. 5-2 (a) and (b). When the coarse glass beads screen is placed at the expanding plane, the disturbance in the flow regime caused by the expansion effect is stabilized. This stabilizing effect is observed only when an adequate applied flow rate ($q \geq 1$ lit/min) is reached. In the range of flow rate tested in this experiment ($0.1 \text{ lit/min} \leq q \leq 8 \text{ lit/min}$), this stabilizing effect becomes more effective as the applied flow rate increases. In contrast, the disturbance is not stabilized as the flow rate increases when no screen is placed at the expanding plane.

The same tendency as the curves in Fig. 5-2 (b) is observed in Fig. 5-2 (c). An exception in Fig. 5-2 (c) appears when $q = 1$ lit/min, the velocity probability distribution range is wider, and the proportion of downwards velocity is larger than that in Fig. 5-2 (b) when $q = 1$ lit/min. This means that when $q = 1$ lit/min, the flow regime is more disturbed when a less permeable screen is placed. This outcome does not agree with the conclusions drawn from previous research works, in which a less permeable screen was considered to stabilize the disturbance caused by the expansion effect more effectively (Chen *et al*, 2008; Assato, Pedras and De Lemos, 2005). However, those previous research works regarding permeability were conducted at a high chamber Reynolds number, i.e. $Re_c = 800$ (Chen *et al*, 2008) or $Re_c = 132000$ (Assato, Pedras and De Lemos, 2005), while this exceptional phenomenon is observed only when $q = 1$ lit/min ($Re_c = 166.67$). A hypothesis to explain this exception is that a low-permeable porous screen can only enhance the stabilizing effect at a relatively high chamber Reynolds number. This hypothesis will be further discussed in 5.1.3.

5.1.2 Velocity distribution in granular medium

As discussed in 4.1.2, velocity vectors can be detected in the regions of an image where hydro-gel beads are present, due to minor displacements caused by the rotation of hydro-gel beads. However, these velocity vectors are not indicating velocity of the micro-scale flow, and are therefore not of interest in this study. Vectors in those regions are excluded from analysis by applying an image mask. The hydro-gel beads regions in the velocity vector field graphs are therefore blank, as shown in Fig. 5-3.

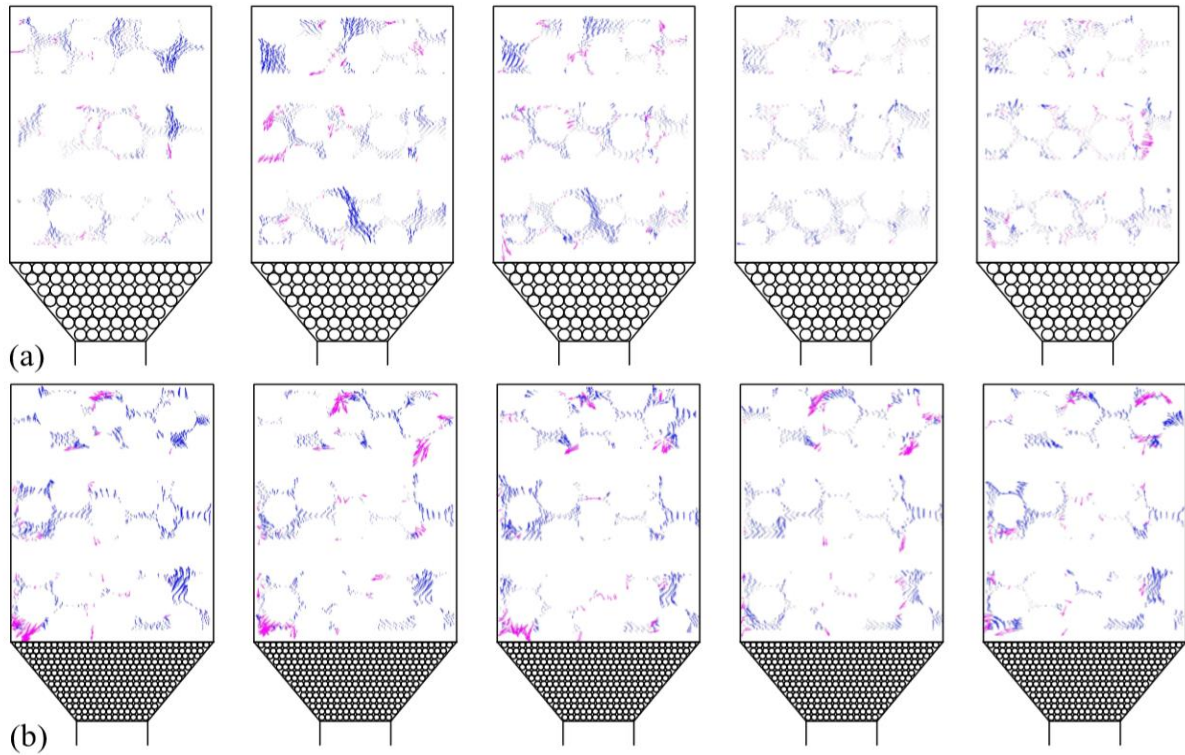


Fig. 5-3 Vector field graphs for different test configurations: **(a)** Group D, granular medium with coarse glass beads screen; and **(b)** Group E, granular medium with fine glass beads screen. With upwards velocity plotted in blue and downwards velocity plotted in magenta. Applied flow rates from left to right: for Group D, 0.1 lit/min ($Re_m = 3$), 1 lit/min ($Re_m = 30$), 2 lit/min ($Re_m = 60$), 4 lit/min ($Re_m = 120$), and 8 lit/min ($Re_m = 240$); for Group E, 0.1 lit/min, 1 lit/min, 2 lit/min, 4 lit/min, and 5 lit/min ($Re_m = 150$)

Fig. 5-3 (a) and (b) are derived from the data obtained with the experimental configurations of Group D and E in Table 4-1, namely a granular medium with coarse glass beads screen and a granular medium with fine glass beads screen, respectively. The granular medium is formed by a pack of 1.8-cm-diameter hydro-gel beads. The applied flow rates are 0.1 lit/min, 1 lit/min, 2 lit/min, 4 lit/min and 8 lit/min for the five vector field graphs in Fig. 5-3 (a) from left to right, respectively. In Fig. 5-3 (b), the highest applied flow rate is 5 lit/min due to the fine glass beads screen's low permeability, as discussed in 4.2.1. The velocity is also normalized with the mean Darcy flow speed, as introduced in 5.1.1. The length scale factors of arrows are the same for all vector field graphs in Fig. 5-3, but are smaller than those in Fig. 5-1. This smaller length scale allows more details to be shown inside the pores among adjacent hydro-gel beads. To be distinguished from the empty chamber configurations in Fig. 5-1, the granular medium

Reynolds number is introduced for this part of discussion, defined as:

$$Re_m = \frac{\rho u_D D}{\mu} \quad (5-4)$$

where D is the diameter of the hydro-gel beads forming the granular medium.

In Fig. 5-3 (a) and (b), the velocity vectors do not show a specific changing pattern as the applied flow rate increases. Comparing with Fig. 5-1, the number of downwards velocity vectors is reduced when $q = 0.1$ lit/min. It can be inferred that the granular medium stabilizes the disturbance caused by the expansion effect when the applied flow rate is low.

However, minor downwards velocity is observed for all flow rate conditions. These minor reverse velocity vectors were also observed in previous research works studying the micro-scale flow in granular media formed by packs of spheres (Peurrung, Rashidi and Kulp, 1995; Lebon *et al*, 1996; Yang *et al*, 2013; Cenedese and Viotti, 1996; Harshani *et al*, 2016; Huang *et al*, 2008; Johns *et al*, 2000; Patil and Liburdy, 2013). These reverse velocity vectors can be caused by wakes induced by the drag force exerted to spheres that form the granular medium, as discussed in 2.1.4. In the current experiment, the wakes are restricted due to the dense packing of hydro-gel beads. Thus, full vortex rings are not observed from the velocity vector field graph, but downwards velocity vectors occur due to the drag force.

To study the velocity distribution, the PDFs are also plotted, as shown in Fig. 5-4. The same method as plotting Fig. 5-2 is used. The velocity magnitude is normalized with the mean Darcy flow speed, u_D , to allow comparison between tests conducted at different applied flow rates.

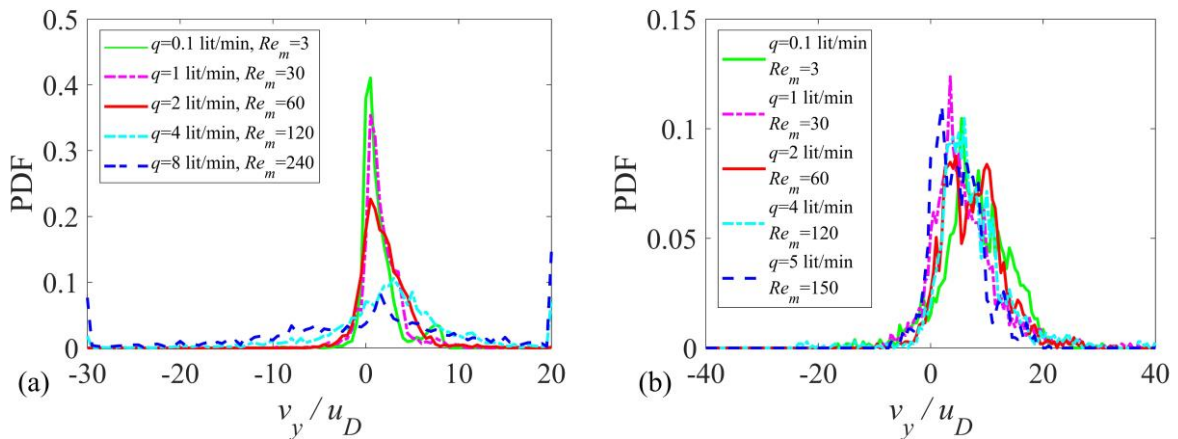


Fig. 5-4 PDF plotting of flow-wise velocity components in the middle section at different applied flow rates for (a) Group D, granular medium with coarse glass beads screen; and (b) Group E, granular medium with fine glass beads screen

The only difference between the experimental configurations of Group B and D is whether a granular medium is placed inside the chamber. Interestingly, different from Fig. 5-2 (b), a concentrated velocity probability distribution is observed for low applied flow rates in Fig. 5-4

(a). In spite of a small proportion of negative velocity caused by the drag force, a sharp increase occurs around $v_y / u_D = 0$ for curves derived from tests conducted at applied flow rates of 0.1 lit/min, 1 lit/min, and 2 lit/min. A peak occurs around $v_y / u_D = 0$ in these curves. As the applied flow rate increases, the velocity probability distribution range becomes wider, and the negative proportion becomes larger. The decay after the peak around $v_y / u_D = 0$ also becomes more gradual for higher applied flow rates. This tendency of the PDF curves matches with those generated in the numerical simulation conducted by Rong, Dong and Yu (2013), as introduced in 2.1.4. When the applied flow rate is higher than 4 lit/min, the curves become flat and cover a wide range, and reach to the negative extent of v_y / u_D . This indicates that the variation in velocity magnitude is significant, and the negative velocity proportion is large. In summary, the velocity distribution patterns observed in Fig. 5-2 (b) at higher applied flow rates ($q \geq 1$ lit/min) are observed in Fig. 5-4 (a) at lower applied flow rates ($q \leq 2$ lit/min), which are featured as the stabilized flow regime; vice versa, the wide-ranged flat curve observed in Fig. 5-2 (b) at a lower flow rate ($q = 0.1$ lit/min) is observed in Fig. 5-4 (a) at higher applied flow rates ($q \geq 4$ lit/min), which are featured as the disturbed flow regime.

By analyzing the PDF curves in Fig. 5-4 (a), conclusions can be drawn as follows. Firstly, despite the negative velocity vectors, the disturbance caused by the expansion effect is stabilized at a low applied flow rate ($q = 0.1$ lit/min) when a granular medium is placed in the chamber. The disturbance is observed under the same porous screen condition but without a granular medium when $q = 0.1$ lit/min. Thus, placing a granular medium in the chamber along the flow path helps stabilize the disturbance caused by the expansion effect. In the numerical simulation conducted by Chen *et al* (2008), the porous screen's stabilizing effect was enhanced as the screen's thickness increased. The granular medium can act as an extension of the porous screen, and increases the thickness, to enhance the stabilizing effect of the porous screen. Secondly, wide-ranged flat curves occur for higher applied flow rates. According to the conclusion drawn from 5.1.1 discussion, the disturbance caused by the expansion effect is considered to be stabilized as the applied flow rate increases. Nevertheless, as discussed in 2.1.4, the minimum Reynolds number for the laminar-turbulent transition to start in flow travelling in granular media can be as low as 90. The PDF curves in Fig. 5-4 (a) recognized to be disturbed occur at a minimum Re_m of 120. In addition, turbulent flow regimes in granular media are featured with vortices and reverse flows (Wegner, Karabelas and Hanratty, 1971). These features also match with the velocity probability distribution in Fig. 5-4 (a) when $q \geq 4$ lit/min. Thus, the disturbance that occurs as the applied flow rate increases can be caused by the laminar-turbulent transition, instead of the expansion effect. However, turbulence cannot be recognized solely according to the proportion of reverse flows. To confirm that this disturbance

is caused by turbulence, additional measurements need to be conducted, such as measuring vorticity distribution in the flow field (Chorin and Chorin, 1994) or pressure drop along the flow path (Han, Park and Ibrahim, 1986). Although remained hypothetical, this disturbed flow regime caused by the increasing applied flow rate is referred to as turbulence in the following discussion. This disturbance in flows travelling through the granular medium that occurs at high Reynolds numbers can then be distinguished from the disturbance caused by the expansion effect.

In Fig. 5-4 (b), when the fine glass beads screen is placed at the expanding plane, the negative proportion in v_y / u_D is also observed. The difference in velocity probability distribution caused by the increasing flow rate is mitigated. The curves' patterns are similar, and the turbulence does not occur at the highest applied flow rates tested ($q = 5$ lit/min). Nevertheless, the fine glass beads screen might not be able to eliminate the turbulence. The hypothetical reason for the absence of turbulence in Fig. 5-4 (b) can be that the critical Re_m for the laminar-turbulent transition to begin is not reached in this test. This hypothesis cannot be proven with the current experimental setup, as the water head is not high enough to overcome the porous screen's low permeability and to allow higher applied flow rates. However, the highest Re_m in Fig. 5-4 (b) to maintain a laminar flow regime reaches 150. This is higher than that in Fig. 5-4 (a), in which critical Re_m is between 60 and 120. Thus, the following conclusions are reached. On the one hand, the fine glass beads screen can mitigate the differences in the flow regime caused by different applied flow rates within the tested range ($0.1 \text{ lit/min} \leq q \leq 5 \text{ lit/min}$). On the other hand, the fine glass beads screen can increase the critical Re_m for laminar-turbulent transition to begin.

To compare the effect of different experimental configurations, the PDFs are plotted with data obtained from tests conducted with different experimental configurations but at the same applied flow rates. In Fig. 5-5 (a), the PDFs are plotted with the data obtained when the applied flow rate is 0.1 lit/min, and 4 lit/min for Fig. 5-5 (b). Each curve in the PDF graphs represents a different experimental configuration: with or without a granular medium, coarse or fine glass beads screen.

In Fig. 5-5 (a), the curves for empty chamber cases (red dashed line and green dash-dot line) show disturbance caused by the expansion effect. The curves are featured with a wide range of velocity probability distribution, and a significant negative proportion in v_y / u_D , as discussed in 5.1.1. For the tests conducted with the chamber filled with a granular medium (blue dotted line and magenta solid line), the negative proportion of v_y / u_D is minor. With this comparison, it can be concluded that the disturbance caused by the expansion effect is stabilized by placing

a granular medium in the chamber along the flow path.

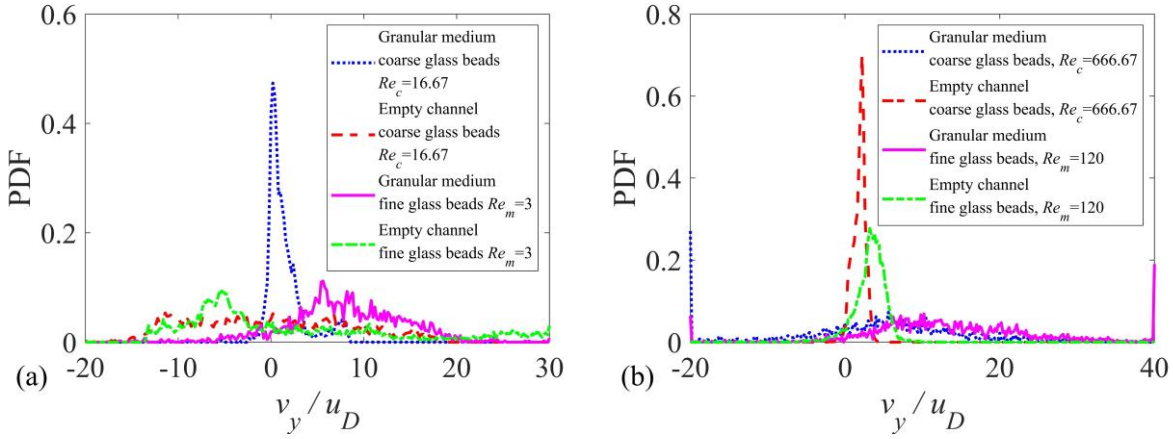


Fig. 5-5 PDF plotting of flow-wise velocity components in the middle section with different experimental configuration at the applied flow rate of (a) $q = 0.1$ lit/min; and (b) $q = 4$ lit/min

In Fig. 5-5 (b), the velocity probability distribution for empty chamber cases becomes concentrated as a higher flow rate is applied. Disturbance in flow regimes caused by the expansion effect is stabilized at this increased chamber Reynolds number. In contrast, a significant negative proportion of v_y/u_D occurs for the granular medium with coarse glass beads screen case, and the velocity probability distribution range becomes wide. This is hypothetically caused by the laminar-turbulent transition, as discussed previously. The negative proportion of v_y/u_D is lower for the granular medium with fine glass beads screen case. The laminar-turbulent transition does not begin at this flow rate ($q = 4$ lit/min) when the fine glass beads screen is placed at the expanding plane. Thus, although the stabilizing effect of porous screens is enhanced by placing a granular medium along the flow path, the laminar-turbulent transition begins at a relatively low applied flow rate. A less permeable porous screen can delay this transition.

5.1.3 Quantitative study of disturbed flow regime

As introduced in 2.3.2, dimensionless parameters were defined to describe the two manifestations of the disturbance caused by the expansion effect: the vortices and reverse flows. Tortuosity has been validated in many previous research works for quantifying the vortices, defined as (Aminpour *et al*, 2018; Duda, Koza and Matyka, 2011; Saomoto and Katagiri, 2015; Jin *et al*, 2015):

$$T = \frac{\sum u}{\sum u_y} \quad (5-5)$$

where u is the magnitude of each velocity vector in the vector field, u_y is the longitudinal (flow-wise) component of u . When no vortex exists, $T_0 = 1$; the higher tortuosity is, the more or larger vortices are.

Tortuosity is plotted versus the applied flow rate in Fig. 5-6. An auxiliary line, $T_0 = 1$ (horizontal thin black line), is also plotted as a reference when no vortex exists. Each curve represents a different experimental configuration. Fig. 5-6 (a) is derived from the data obtained at the entrance section of the chamber, and (b) at the middle section. The numerical results are listed in **Table 0-1** A summary of test results for tortuosityTable 0-1 in Appendices.

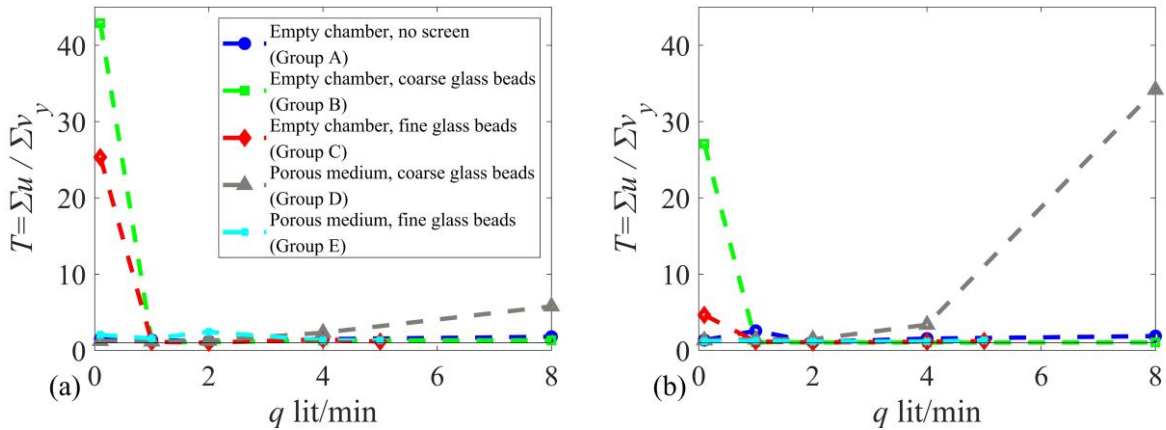


Fig. 5-6 Tortuosity versus applied flow rate for different experimental configuration at the (a) Entrance section; and (b) Middle section of the chamber; (a) and (b) share the same legend

In the tests conducted with an empty chamber with a porous screen placed at the expanding plane (Group B and C configurations), tortuosity is high when $q = 0.1$ lit/min. The high tortuosity indicates that vortices exist, and that the flow regime is disturbed by the expansion effect. When $q \geq 1$ lit/min, tortuosity reduces significantly to around 1. It indicates that few vortices exist, and that the disturbance caused by the expansion effect is stabilized as the applied flow rate increases. This matches with the conclusion drawn from the velocity vector field graphs and the PDF graphs in the 5.1.1 discussion.

In comparison between Fig. 5-6 (a) and (b), when a porous screen is placed at the expanding plane of an empty chamber (Group B and C configurations), tortuosity is lower at the middle section of the chamber. Thus, vortices are mitigated as the flow develops along the longitudinal direction in an empty chamber. Also, tortuosity is lower at both sections of the chamber when the fine glass beads screen is placed than when the coarse glass beads screen is placed. Thus, the less permeable screen is more effective in mitigating the vortices caused by the expansion effect.

In contrast, in the tests conducted when the chamber is filled with the granular medium, and a coarse glass beads screen is placed at the expanding plane (Group D configuration), tortuosity is low when $q \leq 2$ lit/min. As the applied flow rate increases, tortuosity becomes higher. This agrees with the conclusion drawn from the velocity vector field graphs and the PDF graphs in the 5.1.2 discussion, that the granular medium can stabilize the disturbance caused by the

expansion effect at a low applied flow rate ($q = 0.1$ lit/min), but the laminar-turbulent transition begins at a relatively low applied flow rate ($q = 4$ lit/min). Different from the empty chamber cases, tortuosity caused by the laminar-turbulent transition is higher at the middle section of the chamber than that at the entrance section. Thus, as flow develops in a granular medium, vortices are intensified.

For the tests conducted when the chamber is filled with the granular medium, and a fine glass beads screen is placed at the expanding plane (Group E configuration), tortuosity is low at all the tested applied flow rates. The variation between different applied flow rates is minor. It agrees with the conclusion drawn from the PDF graphs in the 5.1.2 discussion, that the less permeable porous screen mitigates the variation in flow regimes at different applied flow rates, and increases the threshold for laminar-turbulent transition to begin.

Interestingly, tortuosity is constantly low when no screen is applied (Group A configuration). It can be seen from Fig. 5-1 (a), although the flow regime is highly disturbed, vortices seldom appear. The main manifestation of the disturbance caused by the expansion effect in this experimental configuration is the reverse streamlines. This indicates that tortuosity alone cannot thoroughly describe the disturbed flow regimes. Thus, the reverse flow speed ratio is introduced for quantifying the downwards velocity, defined as (Back and Roschke, 1972):

$$\alpha = \frac{q^-}{q} = \frac{\left(\frac{\sum u_y^-}{n_t}\right)}{u_D} \quad (5-6)$$

where u_D is the mean Darcy flow speed introduced in 5.1.1, q is the applied flow rate, q^- is the reverse flow rate, and is calculated by averaging the longitudinal components of reverse flow speed, u_y^- , by the total number of detected velocity vectors, n_t . When no reverse flow exists, $\alpha = 0$. The larger α is, the more or faster the reverse flows are.

The reverse speed ratio is plotted versus the applied flow rate in Fig. 5-7. Each curve represents a different experimental configuration. Fig. 5-7 (a) is derived from the data obtained at the entrance section of the chamber, and Fig. 5-7 (b) at the middle section. The numerical results are listed in Table 0-2 in Appendices **Table 0-1** A summary of test results for tortuosity.

The tendencies of α plotting derived from the Group B and D configurations are similar with that of T . The previous conclusions reached for these two configurations about vortices therefore also apply to reverse flows. Thus, when a coarse glass beads screen is placed at the expanding plane, the reverse flow decays as the flow develops along the flow-wise direction in an empty chamber. In contrast, the reverse flow is severer as the flow develops along the flow-wise direction in a granular medium. As vortices and reverse flows are two manifestations of

the disturbance caused by the expansion effect, the following conclusion can be reached. The disturbance caused by the expansion effect in an empty chamber is stabilized as the flow develops along the flow-wise direction. It matches with the results in previous research works (Stieglmeier *et al*, 1989), as discussed in 142.3.3. Similarly, the turbulence that occurs at high Reynolds numbers for flows in a granular medium is intensified as the flow develops along the flow-wise direction.

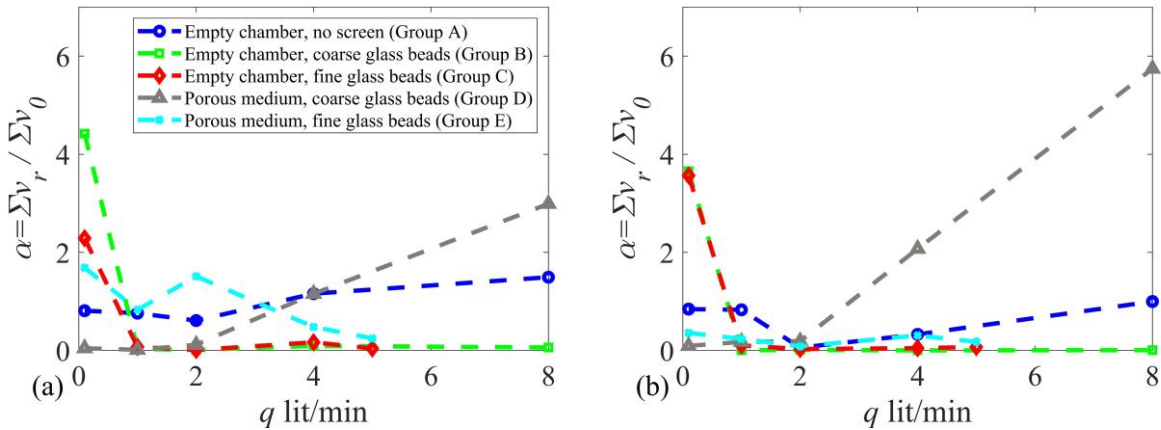


Fig. 5-7 Reverse flow velocity ratio versus applied flow rate for different experimental configuration at the (a) Entrance section; and (b) Middle section of the chamber; (a) and (b) share the same legend

As expected, reverse flow velocity occurs at all tested applied flow rates when no porous screen is placed at the expanding plane of an empty chamber (Group A configuration). Noticeably, when $q \geq 2$ lit/min, the reverse flow speed ratios at the middle section of the chamber are much lower than those at the entrance section of the chamber. This phenomenon is not observed when $q \leq 1$ lit/min. Thus, on the one hand, it agrees with the conclusion drawn previously that the disturbance stabilizes as the flow develops along the flow-wise direction in an empty chamber. On the other hand, as this phenomenon is only observed at higher applied flow rates ($q \geq 2$ lit/min), it indicates that this stabilizing effect of flow development along the flow-wise direction is enhanced by the increasing applied flow rate.

Relatively high reverse flow speed ratios occurs at the entrance section for the Group E configuration when $q \leq 2$ lit/min. The hypothetical laminar-turbulent transition is not reached when $q \leq 2$ lit/min according to the corresponding velocity vector graphs and the PDF curves. However, this high reverse flow speed ratio is not observed at higher flow rates in Fig. 5-7 (a). Also, the reverse flow speed ratios are higher at the entrance section than those at the middle section. As discussed previously, the granular medium can stabilize the disturbance caused by the expansion effect, but can intensify vortices and reverse flows caused by turbulence. Thus, the high reverse flow speed ratios when $q \leq 2$ lit/min can be caused by the expansion effect. The hypothesis developed in 5.1.1 is proven by this result: a low-permeable porous screen is

only effective in stabilizing the disturbance caused by the expansion effect at a relatively high Reynolds number.

For the empty chamber with fine glass beads screen (Group C) configuration, the reverse flow speed ratio when $q = 0.1$ lit/min is higher at the middle section than that at the entrance section. This result is contradictory to the conclusion drawn from the previous discussion and from previous research works (Chen *et al.*, 2008; Assato, Pedras and De Lemos, 2005): the disturbance caused by the expansion effect is stabilized as the flow develops along the empty chamber. This disagreement does not occur for tortuosity, where all the velocity information is derived from the PIV measurement. In calculating the reverse flow speed ratio, the mean Darcy velocity is involved, derived from the flow rate measured with the digital flowmeter. Nevertheless, the precision level of this digital flowmeter is 0.1 lit/min. Thus, when the desired flow rate is 0.1 lit/min, uncertainty in measurement is likely to occur. The testing results can deviate significantly from the actual flow rate. Thus, this disagreement can be caused by the uncertainty in flow rate measurement with the flowmeter.

5.1.4 Limitations of the study

There are limitations in the study of the expansion effect.

The most significant limitation is the error in the flow rate measurement. The flowmeter used in the experiment is the MagMaster flowmeter produced by ABB Group, with a precision level of 0.1 lit/min. Thus, as discussed in 5.1.3, the measurement may not be accurate when the desired flow rate is as low as 0.1 lit/min. This error in measurements leads to faulty results in the reverse flow speed ratio when $q = 0.1$ lit/min. This uncertainty is also observed from the PDF graphs shown in Fig. 5-4 (b), where the curve representing $q = 0.1$ lit/min (green solid line) slightly deviates from the other curves.

Another limitation is that vorticity distribution in the flow field or the pressure drop along the flow path was not measured. It requires additional devices or PIV algorithms. Therefore, the hypothesis developed in 5.1.2 remains untested: the flows travelling through granular media are disturbed by turbulence at high Reynolds numbers.

In addition, flow rates higher than 5 lit/min cannot be reached with the current water head when the fine glass beads screen is placed at the expanding plane. The current water head is not high enough to overcome the low permeability of the fine glass beads screen, as discussed in 4.2.1. Thus, the hypothesis developed in 5.1.2 remains untested: the fine glass beads screen might not be able to eliminate the turbulence, but only increases the critical Re_m for the laminar-turbulent transition to begin. Raising the current water head involves much work, and is not permitted by

the project duration.

5.2 Contact erosion initiation

5.2.1 Experimental setup

As the disturbance caused by the expansion effect is stabilized, a uniform flow is applied to the testing section as the boundary condition for testing the initiation of contact erosion. The experimental setup for the study on the contact erosion initiation is shown with Fig. 4-1. As introduced in 4.2.2, this experimental setup designed benefits from conclusions drawn from the first part of study in the expansion effect.

Two measures are taken to stabilize the disturbed flow regimes with this experimental setup. Firstly, the testing section formed by the hydro-gel beads and glass beads is fixed at the middle section of the chamber with a grid. The flow regime at the middle section in an empty chamber is observed to be more stable, as discussed in 5.1.3. Secondly, a porous screen formed by 5-mm-diameter glass beads is placed in the conical opening at the bottom of the chamber as a porous screen. To initiate the dislodgement of base particles in this experimental setup, the applied flow rate usually needs to be higher than 10 lit/min. Thus, on the one hand, the 5-mm-diameter glass beads screen stabilizes the disturbance caused by the expansion effect at this flow rate; on the other hand, the porous screen is adequately permeable to allow the required flow rates with the current water head.

The uniformity of the boundary condition is confirmed through pre-tests. The flow in the void area below the testing section in the chamber is observed to be upwards and constant along the x -axis (the direction perpendicular to the flow-wise direction) at all the flow rate applied in pre-tests.

Indeed, the flow at the interface between the hydro-gel beads layer and the glass beads layer in the testing section is likely to be turbulent after travelling through the glass beads layer, due to the drag force introduced in 2.1.4. However, the drag force will also occur in a similar circumstance in natural contact erosion. Thus, as long as the boundary condition is uniform, the turbulent flow regime caused by the drag force is acceptable in this experiment.

Fig. 5-8 shows an example of the experimental results in the form of a velocity vector field graph. The green arrows are velocity vectors, with the lengths of arrows proportional to the velocity magnitude. The blue solid circles are the filter particles, and the gray ones are the base particles. Two examples of L_p are given in the graph. The critical pore flow speed, u_f , is the mean flow speed along the pore throat at the moment when dislodgement begins.

The blue solid circles representing filter particles in Fig. 5-8 are in different sizes. This is because the experimental arrangement is three-dimensional, but the light sheet generated by the LED head is only two-dimensional. An example of such three-dimensional arrangement is shown in Fig. 5-9 (a), where the blue spheres are filter particles, the red sphere is a base particle, and the white plane is the light sheet generated by the LED light head. The light sheet only moves along the z -axis, and is always parallel with the xy -plane. When the centers of two filter particles are not in the same xy -plane, the light sheet cannot illuminate the central cross-sections of both filter particles at the same time. As the images acquired with the PIV system are the areas illuminated by the LED light sheet, the image to be acquired from the arrangement in Fig. 5-9 (a) is shown in Fig. 5-9 (b), in which two filter particles appear to be in different sizes.

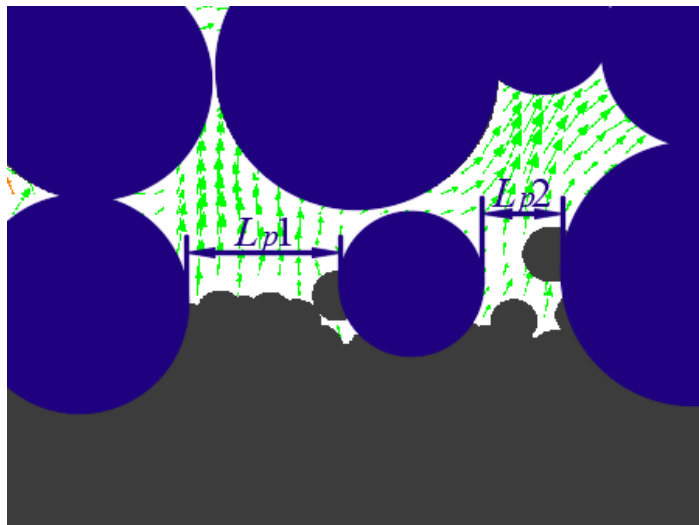


Fig. 5-8 Velocity vector field graph generated with PIVView 2C, showing velocity vectors (green arrows), filter particles (blue solid circles) and base particles (gray solid circles)

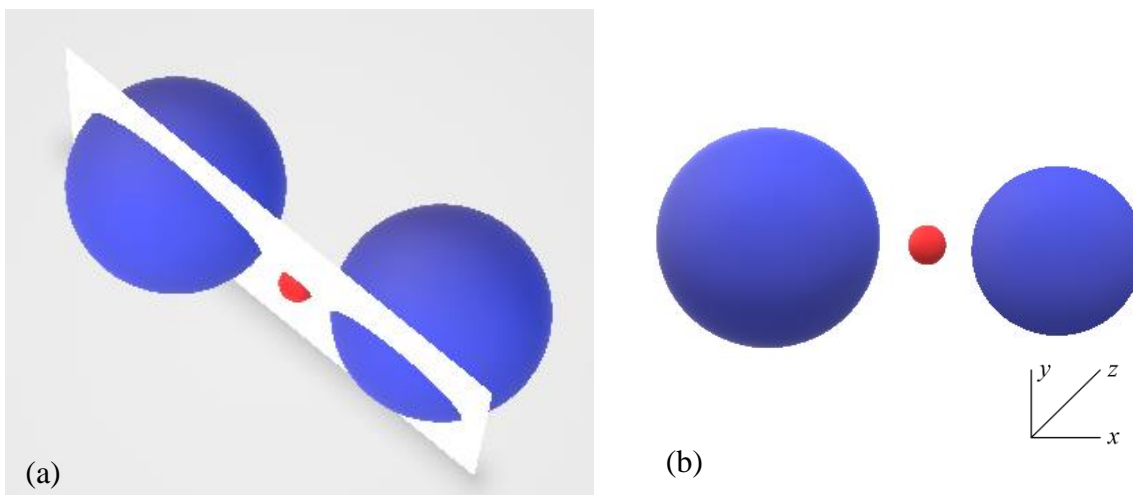


Fig. 5-9 (a) An inclined top view; and (b) A PIV system's view of filter particles (blue sphere), base particles (red sphere), and the light sheet (white plane)

5.2.2 Normalization of velocity data

Fig. 4-4 (b) presents a force analysis of a single base particle in the flow field, where F_D is the

drag force, F_G' is the net force of gravity, the friction force, and the buoyancy force. The buoyancy force and gravity are fixed for a base particle, but the friction force is largely influenced by the geometrical condition in this study (Harshani, 2017). The higher friction force is exerted to the base particle, the higher drag force is required to reach the balance, and therefore the higher pore flow speed is required to trigger the dislodgement. Thus, this friction force can be studied by measuring the critical pore flow speed to trigger contact erosion, u_f . The friction force is therefore omitted in the following calculation of F_G' , and manifests as variation in the measuring results of u_f .

Thus, F_G' can be calculated with:

$$\begin{aligned} F_G' &= F_G - F_B = \rho_p V_p g - \rho V_p g = (\rho_p - \rho) V_p g \\ &= \frac{4\pi}{3} (\rho_p - \rho) \left(\frac{D_b}{2}\right)^3 g = \frac{\pi}{6} (\rho_p - \rho) D_b^3 g \end{aligned} \quad (5-7)$$

Where F_G and F_B are gravity and the buoyancy fore respectively, ρ_p and ρ are the base particle density and water density respectively, V_p is the volume of a base particle.

F_D in Fig. 4-4 (b) is the drag force, and can be calculated with (Tsuji, Kato and Tanaka, 1991):

$$F_D = C_D \frac{\pi}{8} D_b^2 \rho u_f^2 - \frac{\pi}{6} D_b^3 \frac{dp}{dx} + f_D \quad (5-8)$$

where dp/dx is the pressure gradient along the x -axis, f_D is the unsteady part of the drag force, C_D is the drag coefficient, calculated with (White and Corfield, 2006):

$$C_D = \frac{24}{Re_p} + \frac{6}{1 + Re_p^{0.5}} + 0.4 \quad (5-9)$$

where Re_p is the particle Reynolds number, defined as:

$$Re_p = \frac{\rho u_f D_b}{\mu} \quad (5-10)$$

where μ is the dynamic viscosity of water.

Apparently, for a base particle in the flow field, F_D increases as the pore flow speed increases. When the critical point $F_D = F_G'$ is reached, the base particle starts to dislodge, and u_f is detected. At this critical point:

$$F_G' = F_D \quad (5-11)$$

$$\frac{\pi}{6} (\rho_p - \rho) D_b^3 g = C_D \frac{\pi}{4} D_b^2 \frac{1}{2} \rho u_f^2 - \frac{\pi}{6} D_b^3 \frac{dp}{dx} + f_D \quad (5-12)$$

In this experiment, a uniform flow is applied. The pressure gradient along the x -axis therefore approaches 0. Also, the unsteady part of the drag force can be ignored, as the magnitude is

minor comparing with other parts of the drag force in Equation (5-8). Therefore:

$$\frac{\pi}{6}(\rho_b - \rho)D_b^3g = C_D \frac{\pi}{8}D_b^2\rho u_f^2 \quad (5-13)$$

and can be simplified as:

$$\frac{4}{3}(\rho_b - \rho)D_bg = C_D\rho u_f^2 \quad (5-14)$$

Define S as the specific gravity of base particles, namely base particles' relative density to water:

$$S = \frac{\rho_p}{\rho} \quad (5-15)$$

Therefore, Equation (5-14) can be rewritten as:

$$\frac{4}{3}(S - 1)D_bg = C_D u_f^2 \quad (5-16)$$

Thus:

$$u_f = \sqrt{\frac{4(S - 1)D_bg}{3C_D}} \propto \sqrt{\frac{(S - 1)D_bg}{C_D}} \quad (5-17)$$

As introduced in 4.2.2, this experiment focuses on the variation in the initiating flow speed caused by different size ratios of L_p / D_b and D_f / D_b . According to Equation (5-8), the size of base particles and the particle Reynolds number influence the drag force acting on a based particle. Base particles of different sizes are used in this experiment. Thus, to make the measuring results obtained with base particles of different sizes comparable, a new parameter needs to be introduced to eliminate the impact caused by different D_b s. This new parameter, Fr_{int} , is defined as:

$$Fr_{int} = u_f \sqrt{\frac{C_D}{(S - 1)D_bg}} \quad (5-18)$$

where C_D is calculated with Equation (5-9). The flow speed data obtained from the PIV measurements is converted into Fr_{int} to be compared between different groups of tests.

Under each geometrical condition, base particles of a certain size and specific gravity are used. This means that S and D_b are constant. Re_p is therefore only related to the measured pore flow speed. Let:

$$C_1 = \frac{\rho D_b}{\mu} \quad (5-19)$$

where C_1 is constant and positive. Re_p can be simplified as:

$$Re_p = C_1 u_f \quad (5-20)$$

Therefore, C_D in Equation (5-9) can be rewritten as:

$$C_D = \frac{24}{u_f} + \frac{6}{1 + (C_1 u_f)^{0.5}} + 0.4 \quad (5-21)$$

Let:

$$C_2 = \frac{1}{\sqrt{(S-1)D_b g}} \quad (5-22)$$

where C_2 is constant and positive. Fr_{int} can be rewritten as:

$$\begin{aligned} Fr_{int} &= C_2 u_f \sqrt{\frac{24}{C_1 u_f} + \frac{6}{1 + (C_1 u_f)^{0.5}} + 0.4} \\ &= \sqrt{\frac{24 C_2^2}{C_1} u_f + \frac{6 C_2^2 u_f^2}{1 + (C_1 u_f)^{0.5}} + 0.4 C_2^2 u_f^2} \end{aligned} \quad (5-23)$$

By further simplifying all the constants in Equation (5-23) with positive constants C_3 , C_4 and C_5 , Fr_{int} in Equation (5-18) can be rewritten as:

$$Fr_{int} = \sqrt{C_3 u_f + \frac{C_4 u_f^2}{1 + (C_1 u_f)^{0.5}} + C_5 u_f^2} \quad (5-24)$$

It can then be easily proven that:

$$\frac{dFr_{int}}{du_f} = \frac{C_3 + \frac{2C_4 u_f + 2C_1^{0.5} C_4 u_f^{2.5}}{1 + C_1 u_f + 2(C_1 u_f)^{0.5}} + 2C_5 u_f}{2 \sqrt{C_3 u_f + \frac{C_4 u_f^2}{1 + (C_1 u_f)^{0.5}} + C_5 u_f^2}} \quad (5-25)$$

All components in Equation (5-25) are positive, thus:

$$\frac{dFr_{int}}{du_f} > 0 \quad (5-26)$$

Thus, Fr_{int} is always positively related to u_f . However, as Equation (5-25) indicates, the slope of a $Fr_{int} - u_f$ plot is related to the magnitude of u_f . In some ranges of u_f , the variation in Fr_{int} may not reflect the variation in u_f in a linear manner; in this case, the dimensionless parameter Fr_{int} is unsuitable for normalizing u_f . Thus, Fr_{int} is not a universal parameter for normalizing u_f of any range. The applicability of Fr_{int} in the range of u_f detected in this experiment will be further discussed in 5.2.3.

Comparing with the dimensionless parameter Fr adopted by Harshani (2017) as shown with

Equation (2-2), the sore difference is that Fr considers C_D as a constant $C_D = 1$. In the numerical simulation, the base particle size was kept constant as 9 mm. The particle Reynolds number therefore only changed with different u_f s. In contrast, base particles of different sizes are used in this study, and therefore the variation range of Re_p can be much larger than that in the numerical simulation. The necessity of considering C_D as a variable in this study will be further discussed in 5.2.3.

5.2.3 Variation in initiating flow speed

The experimental results obtained from different configurations are processed and listed in Table 0-3, as attached in Appendices.

With the experimental results listed in Table 0-3, Fr_{int} calculated with Equation (5-18) is plotted versus u_f in the ranges of u_f results obtained with each geometrical configuration, as shown in Fig. 5-10. As discussed in 5.2.2, Fr_{int} is not a universal parameter suitable for normalizing u_f in any circumstance. Each curve in Fig. 5-10 represents one geometrical condition. All the curves representing different geometrical configurations in Fig. 5-10 show that Fr_{int} is roughly linearly dependent on u_f within the range of u_f results; in other words, variation in Fr_{int} can reflect the variation in u_f in a roughly linear manner in this study. Thus, Fr_{int} defined with Equation (5-18) is applicable for normalizing u_f in this study. Also, the slopes are different for different curves in Fig. 5-10: when smaller base particles are used, the corresponding curve has a sharper increase. According to Equation (5-17), u_f is positively related to D_b . In other words, the pore flow speed required to trigger the dislodgement of fine particles is lower when D_b is smaller. This is the reason why u_f is not directly comparable for different geometrical configurations: it is not only influenced by the friction force that relates to the filter particles' arrangement, but also influenced by the size of base particles. A sharper increase in Fr_{int} for a smaller D_b overcomes this difference in u_f caused by different base particle sizes, and guarantees that Fr_{int} is comparable.

The necessity of considering C_D as a variable is also discussed 5.2.2. C_D is plotted versus Re_p in Fig. 5-11 within the range of Re_p listed in Table 0-3. The variation in C_D cannot be ignored in this range of Re_p . Thus, it is necessary to consider C_D as a variable in this study.

The measuring results in Table 0-3 is scattered in Fig. 5-12. Each form of dots represents one geometrical configuration. The coordinate of each dot is derived from one single test. The y-coordinate of each dot is calculated with Equation (5-18).

In Fig. 5-12, minor contrast is observed between blue dots and red dots. The initiating pore flow speed therefore does not vary much with different absolute sizes of filter and base particles. It

indicates that Fr_{int} can effectively eliminate the impact caused by different particle sizes. Also, the difference between different forms of dots is slight. The initiating pore flow speed therefore does not vary much as D_f/D_b changes. The initiating flow speed only changes significantly due to variation in the pore throat length in this experiment.

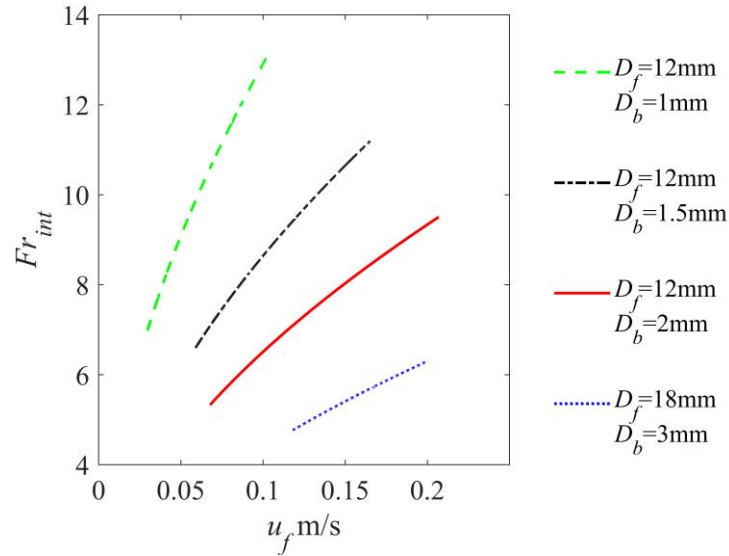


Fig. 5-10 Fr_{int} versus u_f for different geometrical configurations in the range of u_f results

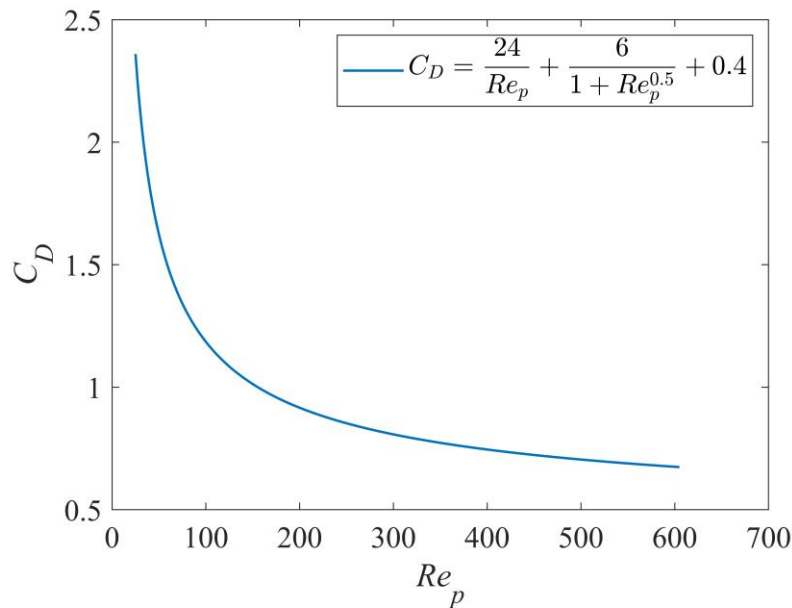


Fig. 5-11 C_D versus Re_p in the range of Re_p results

The tendency in Fig. 5-12 is similar with the numerical results presented in Fig. 2-5 (c). The difference between Equation (2-2) and (5-9) is that the drag coefficient is considered as constant $C_D = 1$ in the definition of Fr in the numerical simulation conducted by Harshani (2017), while C_D is considered as a variable in this study. According to Re_p data listed in Table 0-3, the magnitude of Re_p is larger for larger D_b s. When 3-mm-diameter base particles are used, Re_p reaches 350 to 600. As shown in Fig. 5-11, C_D remains relatively steady in this range of Re_p .

In the numerical simulation, D_b was constantly kept as 9 mm. It can be inferred that when $D_b = 9$ mm, the variation in C_D calculated with Equation (5-9) is so minor, that C_D can be considered as constant. Thus, Fr_{int} is linearly comparable with Fr when $D_b = 9$ mm. Sill, C_D calculated with Equation (5-9) is much smaller than 1 when $D_b = 9$ mm. This explains why similar tendencies occur for numerical and experimental results, but a downwards shift occurs for Fr_{int} comparing with Fr .

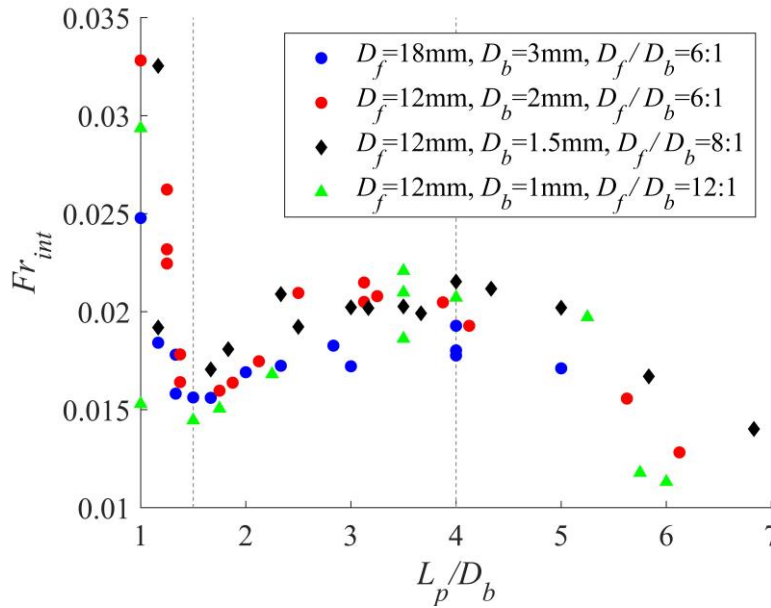


Fig. 5-12 Fr_{int} variation for different geometrical configurations

A general tendency for all the four groups of tests is summarized as follows. Two turning points occur at $L_p / D_b = 1.5$ and $L_p / D_b = 4$, where auxiliary lines (gray dashed lines) are plotted. A similar tendency was also observed in the numerical simulation conducted by Harshani (2017). The curves were divided into three zones according to the tendency of variation as shown in Fig. 2-5 (c). The three zones also occur in Fig. 5-12. The three zones are $1 < L_p / D_b < 1.5$, $1.5 < L_p / D_b < 4$, and $L_p / D_b > 4$ for Zone 1, Zone 2, and Zone 3 respectively.

In Zone 1, when L_p / D_b approaches 1, the pore throat length is similar to the base particle's diameter. The geometrical condition therefore poses great restriction on the base particle's movement. Correspondingly, the initiating pore flow speed to trigger dislodgement of the base particles is high when L_p / D_b approaches 1. This restriction reduces as the pore throat grows wider, and the initiating flow speed decreases correspondingly, and reaches a valley when $L_p / D_b = 1.5$. In addition, a jet-like flow pattern was observed at the top of the base particle bed in the numerical simulation. This jet-like flow pattern is formed due to the geometrical condition at this stage, as shown in Fig. 2-5 (d). This jet-like flow pattern was considered to accelerate the initial dislodgement of base particles (Harshani, 2017).

In Zone 2, the accelerating effect of the jet-like flow pattern begins to diminish. The initiating flow speed therefore increases again. This growth ends when $L_p / D_b = 4$, where a peak is reached.

Difference between the experimental results and the numerical results occurs in Zone 3. In the numerical model, the initiating flow speed remained constant after reaching the peak at $L_p / D_b = 4$, demonstrating that the dislodgement was no longer influenced by the geometrical condition (Harshani, 2017). Nevertheless, in Fig. 5-12, a slight decrease occurs in Zone 3. This decrease in Fr_{int} in Zone 3 may be attributed to the undetected three-dimensional filter particle arrangement along the z -axis, as shown in Fig. 5-13 (a). The blue spheres A, B, C and D represent filter particles, and the red sphere represents a base particle. As particle A and B become apart, the space between them becomes larger, and therefore particle C and D along the z -axis are more likely to approach the observed base particles, as shown in Fig. 5-13 (b). In this way, particle C and D exert their impact on the base particles' motion. The same jet-like flow pattern occurs in Zone 1 may also occur under this geometrical condition, and accelerates the initial dislodgement of base particles. In addition, as the void between particle A and B provides adequate space for the base particle to move, the restriction posed by the geometrical condition is not so significant in Zone 3 comparing with that in Zone 1. Thus, the lowest Fr_{int} in Zone 3 is even lower than the valley of Fr_{int} at $L_p / D_b = 1.5$. As discussed in 5.2.1, the view observed from the PIV system is restricted to the area illuminated by the LED head. Therefore, the geometrical configuration along the z -axis cannot be seen, as the LED head only illuminates areas in the xy -plane. The view observed from the PIV system is as shown in Fig. 5-13 (c). Such problem can be avoided in a numerical simulation with a three-dimensional view, but cannot be detected nor solved with the current experimental setup.

Another difference between the experimental and numerical results is that the whole curve is translated along the y -axis: Fr in the numerical simulation ranged from approximately 0.2 to 0.5, and Fr_{int} in the current experiment ranges from approximately 0.015 to 0.035. One possible reason for the difference is explained previously, that the drag coefficient is considered as constant $C_D = 1$ in Equation (2-2), but C_D calculated with Equation (5-9) is much smaller than 1 when $D_b = 9$ mm, according to Fig. 5-11. Thus, the drag coefficient in the numerical simulation is much larger than that in the experiment. Another possible reason for the deviation is that the numerical model simulated soil particles, but the current experiments are conducted with glass beads. The friction force between base particles are therefore different for the numerical model and the experiment configuration. A smaller friction between glass beads can lead to a lower initiating flow speed. This difference in friction force also explains the

downwards shift of Fr_{int} comparing with Fr .

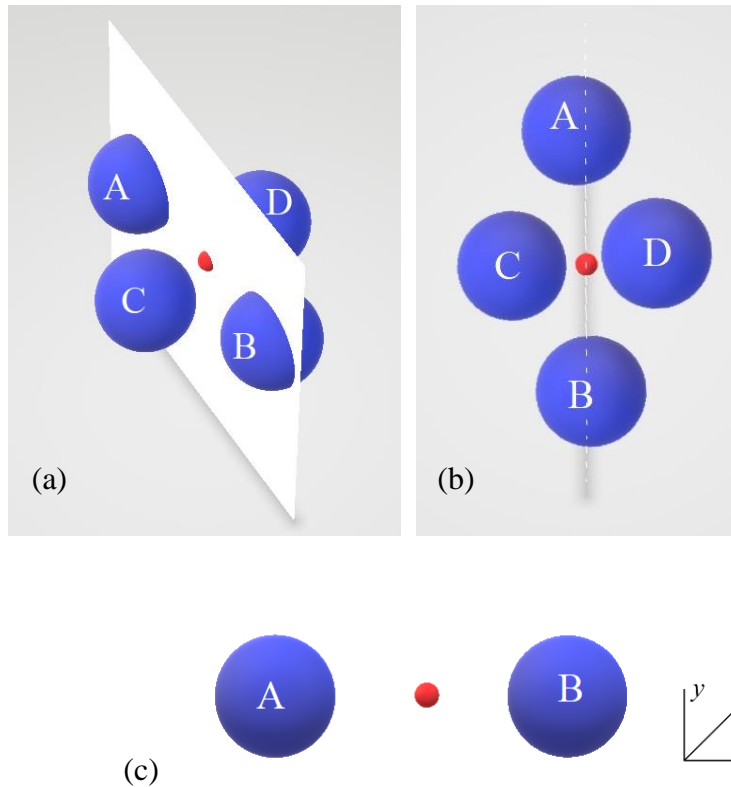


Fig. 5-13 (a) An inclined top view; (b) a top view; and (c) A PIV system's view of filter particles (blue sphere), base particles (red sphere), and the light sheet (white plane)

Despite the deviation from numerical results, the variation in Fr_{int} as L_p / D_b changes indicates that L_p / D_b significantly influence the flow condition to initiate dislodgement of base particles. At a field scale, L_p / D_b is related to porosity of coarse-particle soil and the particle size of fine-particle soil. The flow condition to initiate dislodgement of base particles reflects the threshold of the applied flow to trigger contact erosion. The micro-scale experimental results therefore matches with the conclusions drawn from the field-scale experiment conducted by Cyril *et al* (2009). Coarse-particle soil's porosity and fine-particle soil's particle size influenced the critical applied flow velocity to trigger contact erosion, as indicated by Equation (2-1).

5.2.4 Limitations of the study

The most significant limitation in this study is the failure in studying the filter particles' influence from a stereo three-dimensional view. As introduced in 5.2.3, with the current two-dimensional PIV system, only a single plane of the testing section can be observed. However, the actual arrangement is three-dimensional, as shown in Fig. 5-9 and Fig. 5-12. The impact in space can significantly influence the flow condition to trigger contact erosion, but is ignored in this study. With the current two-dimensional PIV detection, the hypothesis proposed in 5.2.3 on the impact exerted by filter particles along the z -axis cannot be tested.

6 Conclusions and Recommendations

This project studied the critical pore flow speed to induce contact erosion under different geometrical arrangements of particles. Stabilizing the disturbance caused by the expansion effect was a secondary yet prior problem in the study to provide a uniform boundary condition. The study focused on the stabilizing effect of porous screens and different flow rates. The impact posed by a granular medium on the flow regime was also studied.

The following conclusions were drawn from the expansion effect study:

- When fluids travel through an empty chamber with a porous screen placed at the expanding plane, the disturbance caused by the expansion effect is significant at low flow rates, but is stabilized as the applied flow rate increases; a low-permeable porous screen only enhances this stabilizing effect at relatively high Reynolds numbers
- When fluids travel through a granular-medium-filled chamber with a porous screen placed at the expanding plane, the disturbance that occurs at low flow rates in an empty chamber is stabilized, but the flow regimes become disturbed at higher Reynolds numbers; hypothetically this disturbance is caused by the laminar-turbulent transition; a low-permeable porous screen can increase the threshold in flow rate for the laminar-turbulent transition to begin
- The disturbance in an empty chamber is stabilized as fluid develops along the flow-wise direction, regardless whether a porous screen is placed at the expanding plane, but the turbulence in a granular-medium-filled chamber intensifies as fluid develops along the flow-wise direction

The conclusions drawn from the expansion effect study contributed to optimizing the experimental setup for the contact erosion study. With this optimized experimental setup, a uniform flow was attained, and applied to the testing section. The experimental configuration conformed to a numerical simulation conducted by Harshani (2017). Experimental results similar to the numerical results were obtained. The conclusions add to knowledge in the triggering mechanism of contact erosion.

The following conclusions were drawn from the contact erosion initiation study:

- Different size ratios between filter and base particles do not impact on the pore flow speed to trigger dislodgement of base particles significantly
- The initiating pore flow speed varies significantly depending on different size ratios between pore throat lengths and base particle diameters

Still, there are limitations in this study. Firstly, the digital flowmeter used in this study has a precision level of only 0.1 lit/min. The measurements of low flow rates may contained uncertainties. Secondly, the vorticity distribution in flow fields and the pressure drop along flow paths were not measured. The hypothesis that flows travelling through granular media are disturbed by turbulence at high Reynolds numbers remained untested. Thirdly, the water head was not high enough to recover the low permeability of fine glass beads screen and attain higher flow rates. The hypothesis that a low-permeable porous screen cannot eliminate turbulence, but only increases the threshold for the laminar-turbulent transition to begin remained untested. At last, the PIV measurement can only observe two-dimensional planes. The hypothesis that the three-dimensional arrangement of filter particles impacts on the initiating pore flow speed also remained untested due to the limitation of the experimental apparatus.

Those limitations also provide future research possibilities. To overcome these limitations, the following improvement are recommended:

- A flowmeter with higher precision should be used for measuring delicate flow rates
- Pressure drop along the flow path can be measured with pressure probes; vorticity distribution can be calculated with advanced PIV algorithms
- The cylinder bucket forming the water head should be raised
- Another set of PIV equipment should be configured to acquire the images in the yz-plane of the chamber

References

- Abdelhamid, Y and El Shamy, U, 2014. Pore-scale modeling of surface erosion in a particle bed, *International Journal for Numerical Analytical Methods in Geomechanics*, 38(2):142-166.
- Achenbach, E, 1974. The effects of surface roughness and tunnel blockage on the flow past spheres, *Journal of Fluid Mechanics*, 65(1):113-125.
- Adrian, R J J A r o f m, 1991. Particle-imaging techniques for experimental fluid mechanics, *Annual Review of Fluid Mechanics*, 23(1):261-304.
- Akselli, B, Kholmatov, A and Nasibov, H, 2009. The use of CCD pixel binning in PIV measurements, paper presented to 2009 International Symposium on Optomechatronic Technologies.
- Aminpour, M, Galindo-Torres, S, Scheuermann, A and Li, L, 2018. Pore-Scale Behavior of Darcy Flow in Static and Dynamic Porous Media, *Physical Review Applied*, 9(6):064025.
- Assato, M, Pedras, M H and De Lemos, M J, 2005. Numerical solution of turbulent channel flow past a backward-facing step with a porous insert using linear and nonlinear k- ϵ models, *Journal of Porous Media*, 8(1).
- Back, L and Roschke, E, 1972. Shear-layer flow regimes and wave instabilities and reattachment lengths downstream of an abrupt circular channel expansion, *Journal of Applied Mechanics*, 39(3):677-681.
- Bardet, J-P, 1994. Observations on the effects of particle rotations on the failure of idealized granular materials, *Mechanics of Materials*, 18(2):159-182.
- Beguín, R, Philippe, P and Faure, Y-H, 2012. Pore-scale flow measurements at the interface between a sandy layer and a model porous medium: Application to statistical modeling of contact erosion, *Journal of Hydraulic Engineering*, 139(1):1-11.
- Brown, P P and Lawler, D F, 2003. Sphere drag and settling velocity revisited, *Journal of Environmental Engineering*, 129(3):222-231.
- Brumby, P E, Sato, T, Nagao, J, Tenma, N and Narita, H, 2015. Coupled LBM–DEM micro-scale simulations of cohesive particle erosion due to shear flows, *Transport in Porous Media*, 109(1):43-60.
- Buchmann, N A, Willert, C E and Soria, J, 2012. Pulsed, high-power LED illumination for tomographic particle image velocimetry, *Experiments in Fluids*, 53(5):1545-1560.
- Budwig, R, 1994. Refractive index matching methods for liquid flow investigations, *Experiments in Fluids*, 17(5):350-355.

Byron, M L and Variano, E A, 2013. Refractive-index-matched hydrogel materials for measuring flow-structure interactions, *Experiments in Fluids*, 54(2):1456.

Cenedese, A and Viotti, P, 1996. Lagrangian analysis of nonreactive pollutant dispersion in porous media by means of the particle image velocimetry technique, *Water Resources Research*, 32(8):2329-2343.

Chang, D and Zhang, L, 2012. Critical hydraulic gradients of internal erosion under complex stress states, *Journal of Geotechnical Geoenvironmental Engineering*, 139(9):1454-1467.

Chang, D, Zhang, L and Cheuk, J, 2014. Mechanical consequences of internal soil erosion, *HKIE Transactions*, 21(4):198-208.

Chen, Q and Li, D, 2003. Computer simulation of solid particle erosion, *Wear*, 254(3-4):203-210.

Chen, X, Yu, P, Winoto, S and Low, H T, 2008. A numerical method for forced convection in porous and homogeneous fluid domains coupled at interface by stress jump, *International Journal for Numerical Methods in Fluids*, 56(9):1705-1729.

Chiang, T, Sheu, T W and Wang, S, 2000. Side wall effects on the structure of laminar flow over a plane-symmetric sudden expansion, *Computers and Fluids*, 29(5):467-492.

Chorin, A J and Chorin, A J, 1994. *Vorticity and turbulence* (New York Berlin : Springer.

Cyril, G, Yves-Henri, F, Rémi, B and Chia-Chun, H, 2009. Contact erosion at the interface between granular coarse soil and various base soils under tangential flow condition, *Journal of Geotechnical and Geoenvironmental Engineering*, 136(5):741-750.

Drikakis, D, 1997. Bifurcation phenomena in incompressible sudden expansion flows, *Physics of Fluids*, 9(1):76-87.

Duda, A, Koza, Z and Matyka, M, 2011. Hydraulic tortuosity in arbitrary porous media flow, *Physical Review E*, 84(3):036319.

Durst, F, Pereira, J and Tropea, C, 1993. The plane symmetric sudden-expansion flow at low Reynolds numbers, *Journal of Fluid Mechanics*, 248:567-581.

Dybbs, A and Edwards, R, 1984. A new look at porous media fluid mechanics—Darcy to turbulent, in *Fundamentals of transport phenomena in porous media*, pp 199-256 (Springer.

Falkovich, G, 2011. *Fluid Mechanics* (United Kingdom: Cambridge University Press - M.U.A.

- Fearn, R, Mullin, T and Cliffe, K, 1990. Nonlinear flow phenomena in a symmetric sudden expansion, *Journal of Fluid Mechanics*, 211:595-608.
- Fischer, A, Sauvage, E and Roehle, I, 2008. Acoustic PIV: Measurement of the acoustic particle velocity using synchronized PIV-technique, *Journal of the Acoustical Society of America*, 123(5):3130.
- Foster, M, Fell, R and Spannagle, M, 2000. The statistics of embankment dam failures and accidents, *Canadian Geotechnical Journal*, 37(5):1000-1024.
- Galindo-Torres, S, Scheuermann, A, Mühlhaus, H and Williams, D, 2015. A micro-mechanical approach for the study of contact erosion, *Acta Geotechnica*, 10(3):357-368.
- Gori, F, Petracchi, I and Angelino, M, 2013. Flow evolution of a turbulent submerged two-dimensional rectangular free jet of air. Average Particle Image Velocimetry (PIV) visualizations and measurements, *International Journal of Heat Fluid Flow*, 44:764-775.
- Grant, I, 1997. Particle image velocimetry: a review, *Proceedings of the Institution of Mechanical Engineers, Part C: Journal of Mechanical Engineering Science*, 211(1):55-76.
- Hagsäter, S, Westergaard, C, Bruus, H and Kutter, J, 2008. Investigations on LED illumination for micro-PIV including a novel front-lit configuration, *Experiments in Fluids*, 44(2):211-219.
- Hall, M and Hiatt, J, 1996. Measurements of pore scale flows within and exiting ceramic foams, *Experiments in Fluids*, 20(6):433-440.
- Hammad, K J, Ötügen, M V and Arik, E B, 1999. A PIV study of the laminar axisymmetric sudden expansion flow, *Experiments in Fluids*, 26(3):266-272.
- Han, J, Park, J S and Ibrahim, M, 1986. Measurement of heat transfer and pressure drop in rectangular channels with turbulence promoters.
- Harshani, H, Galindo-Torres, S, Scheuermann, A and Muhlhaus, H, 2016. Experimental study of porous media flow using hydro-gel beads and LED based PIV, *Measurement Science and Technology*, 28(1):015902.
- Harshani, H M D, 2017. *Micro-scale flow and induced contact erosion in granular media*.
- He, Z, Zhong, W, Wang, Q, Jiang, Z and Shao, Z, 2013. Effect of nozzle geometrical and dynamic factors on cavitating and turbulent flow in a diesel multi-hole injector nozzle, *International Journal of Thermal Sciences*, 70:132-143.
- Ho, C C, 2007. The erosion behavior of revetment using geotextile, Université Joseph-Fourier-Grenoble I.

Holdich, R G, 2002. *Fundamentals of Particle Technology* (Midland Information Technology and Publishing: Loughborough, U.K.).

Huang, A Y, Huang, M Y, Capart, H and Chen, R-H, 2008. Optical measurements of pore geometry and fluid velocity in a bed of irregularly packed spheres, *Experiments in Fluids*, 45(2):309-321.

Jin, Y, Dong, J, Li, X and Wu, Y, 2015. Kinematical measurement of hydraulic tortuosity of fluid flow in porous media, *International Journal of Modern Physics C*, 26(02):1550017.

Johns, M, Sederman, A, Bramley, A, Gladden, L and Alexander, P, 2000. Local transitions in flow phenomena through packed beds identified by MRI, *AIChE journal*, 46(11):2151-2161.

Jolls, K and Hanratty, T, 1966. Transition to turbulence for flow through a dumped bed of spheres, *Chemical Engineering Science*, 21(12):1185-1190.

Latifi, M, Midoux, N, Storck, A and Gence, J, 1989. The use of micro-electrodes in the study of the flow regimes in a packed bed reactor with single phase liquid flow, *Chemical Engineering Science*, 44(11):2501-2508.

Lebon, L, Leblond, J, Hulin, J-P, Martys, N and Schwartz, L, 1996. Pulsed field gradient NMR measurements of probability distribution of displacement under flow in sphere packings, *Magnetic Resonance Imaging*, 14(7-8):989-991.

Lo, H-C J, Tabe, K, Iskander, M and Yoon, S-H, 2009. A transparent water-based polymer for simulating multiphase flow, *Geotechnical Testing Journal*, 33(1):1-13.

Meinicke, S, Möller, C-O, Dietrich, B, Schlüter, M and Wetzels, T, 2017. Experimental and numerical investigation of single-phase hydrodynamics in glass sponges by means of combined μ PIV measurements and CFD simulation, *Chemical Engineering Science*, 160:131-143.

Melling, A, 1997. Tracer particles and seeding for particle image velocimetry, *Measurement Science Technology*, 8(12):1406.

Moroni, M and Cushman, J H, 2001. Statistical mechanics with three-dimensional particle tracking velocimetry experiments in the study of anomalous dispersion. II. Experiments, *Physics of Fluids*, 13(1):81-91.

Patil, V A and Liburdy, J A, 2013. Flow characterization using PIV measurements in a low aspect ratio randomly packed porous bed, *Experiments in Fluids*, 54(4):1497.

Peurrung, L M, Rashidi, M and Kulp, T J, 1995. Measurement of porous medium velocity fields and their volumetric averaging characteristics using particle tracking velocimetry, *Chemical Engineering Science*, 50(14):2243-2253.

Raffel, M, Willert, C E, Scarano, F, Kähler, C J, Wereley, S T and Kompenhans, J, 2018. *Particle image velocimetry: a practical guide* (Springer).

Rode, S, Midoux, N, Latifi, M, Storck, A and Saadjian, E, 1994. Hydrodynamics of liquid flow in packed beds: an experimental study using electrochemical shear rate sensors, *Chemical Engineering Science*, 49(6):889-900.

Rong, L, Dong, K and Yu, A, 2013. Lattice-Boltzmann simulation of fluid flow through packed beds of uniform spheres: Effect of porosity, *Chemical Engineering Science*, 99:44-58.

Roy, V, Majumder, S and Sanyal, D, 2010. Analysis of the turbulent fluid flow in an axisymmetric sudden expansion, *International Journal of Engineering Science Technology*, 2(6):1569-1574.

Salomons, S, Hayes, R, Poirier, M and Sapoundjiev, H, 2004. Modelling a reverse flow reactor for the catalytic combustion of fugitive methane emissions, *Computers and Chemical Engineering*, 28(9):1599-1610.

Sankar, S, Kamemoto, D and Bachalo, W, 1992. An evaluation on the use of large, hollow micro-balloons as LDV seed particles, AEROMETRICS INC SUNNYVALE CA.

Saomoto, H and Katagiri, J, 2015. Particle shape effects on hydraulic and electric tortuosities: A novel empirical tortuosity model based on van genuchten-type function, *Transport in Porous Media*, 107(3):781-798.

Shepherd, R G, 1989. Correlations of permeability and grain size, *Groundwater*, 27(5):633-638.

Souza, P V S, Girardi, D and de Oliveira, P M C, 2017. Drag force in wind tunnels: A new method, *Physica A: Statistical Mechanics and its Applications*, 467(C):120-128.

Stieglmeier, M, Tropea, C, Weiser, N and Nitsche, W, 1989. Experimental investigation of the flow through axisymmetric expansions, *Journal of Fluids Engineering*, 111(4):464-471.

Taneda, S, 1956. Experimental Investigation of the Wake behind a Sphere at Low Reynolds Numbers, *Journal of the Physical Society of Japan*, 11(10):1104-1108.

Tsuji, Y, Kato, N and Tanaka, T, 1991. Experiments on the unsteady drag and wake of a sphere at high Reynolds numbers, *International Journal of Multiphase Flow*, 17(3):343-354.

Wegner, T H, Karabelas, A J and Hanratty, T J, 1971. Visual studies of flow in a regular array of spheres, *Chemical Engineering Science*, 26(1):59-63.

Weitzman, J S, Samuel, L C, Craig, A E, Zeller, R B, Monismith, S G and Koseff, J R, 2014. On the use of refractive-index-matched hydrogel for fluid velocity measurement within and

around geometrically complex solid obstructions, *Experiments in Fluids*, 55(12):1862.

White, F M and Corfield, I, 2006. *Viscous fluid flow* (McGraw-Hill New York).

Wiederseiner, S, Andreini, N, Epely-Chauvin, G and Ancey, C, 2011. Refractive-index and density matching in concentrated particle suspensions: a review, *Experiments in Fluids*, 50(5):1183-1206.

Willert, C, Stasicki, B, Klinner, J and Moessner, S, 2010. Pulsed operation of high-power light emitting diodes for imaging flow velocimetry, *Measurement Science Technology*, 21(7):075402.

Yang, X, Scheibe, T D, Richmond, M C, Perkins, W A, Vogt, S J, Codd, S L, Seymour, J D and McKinley, M I, 2013. Direct numerical simulation of pore-scale flow in a bead pack: Comparison with magnetic resonance imaging observations, *Advances in Water Resources*, 54:228-241.

Appendices: Result Tables

Table 0-1 A summary of test results for tortuosity

Medium condition	Screen condition	Group #	q (lit/min)	Re_c or Re_m	T	
					Entrance	Middle
Empty chamber	None	Group A	0.1	16.67	1.472	1.362
			1	166.67	1.379	2.584
			2	333.33	1.194	1.113
			4	666.67	1.495	1.563
			8	1333.33	1.800	1.888
	Coarse glass beads $d = 5$ mm	Group B	0.1	16.67	42.892	27.083
			1	166.67	1.111	1.088
			2	333.33	1.088	1.058
			4	666.67	1.312	1.045
			8	1333.33	1.332	1.057
	Fine glass beads $d = 1$ mm	Group C	0.1	16.67	25.328	4.659
			1	166.67	1.135	1.179
			2	333.33	1.038	1.063
			4	666.67	1.465	1.145
			5	833.33	1.171	1.242
Granular medium	Coarse glass beads $d = 5$ mm	Group D	0.1	3.33	1.254	1.332
			1	33.33	1.188	1.443
			2	66.67	1.273	1.472
			4	133.33	2.333	3.378
			8	266.67	5.784	34.167
	Fine glass beads $d = 1$ mm	Group E	0.1	3.33	2.050	1.198
			1	33.33	1.569	1.274
			2	66.67	2.442	1.169
			4	133.33	1.324	1.182
			5	166.67	1.362	1.344

Table 0-2 A summary of test results for reverse flow ratio

Medium condition	Screen condition	Group #	q (lit/min)	Re_c or Re_m	α	
					Entrance	Middle
Empty chamber	None	Group A	0.1	16.67	0.811	0.844
			1	166.67	0.761	0.830
			2	333.33	0.611	0.059
			4	666.67	1.159	0.329
			8	1333.33	1.494	1.000
	Coarse glass beads $d = 5$ mm	Group B	0.1	16.67	4.420	3.655
			1	166.67	0.031	0.006
			2	333.33	0.011	0.015
			4	666.67	0.095	0.002
			8	1333.33	0.062	0.008
	Fine glass beads $d = 1$ mm	Group C	0.1	16.67	2.288	3.567
			1	166.67	0.073	0.103
			2	333.33	0.010	0.031
			4	666.67	0.167	0.047
			5	833.33	0.004	0.071
Granular medium	Coarse glass beads $d = 5$ mm	Group D	0.1	3.33	0.046	0.094
			1	33.33	0.015	0.176
			2	66.67	0.118	0.190
			4	133.33	1.157	2.074
			8	266.67	2.990	5.744
	Fine glass beads $d = 1$ mm	Group E	0.1	3.33	1.688	0.359
			1	33.33	0.829	0.238
			2	66.67	1.513	0.086
			4	133.33	0.048	0.305
			5	166.67	0.248	0.177

Table 0-3 A summary of test results for contact erosion initiation, unit for u_f : m/s

Case #	L_p / D_b	u_f	Fr_{int}	Re_p	Case #	L_p / D_b	u_f	Fr_{int}	Re_p
F1 $D_b = 1$ mm $D_f = 12$ mm	1.00	0.104	0.029	104.3	F4 $D_b = 3$ mm $D_f = 18$ mm	1.00	0.200	0.025	600.9
	1.00	0.045	0.015	44.8		1.17	0.143	0.018	428.7
	1.50	0.042	0.015	41.5		1.33	0.120	0.016	359.7
	1.75	0.044	0.015	43.8		1.33	0.138	0.018	412.5
	2.25	0.051	0.017	50.8		1.50	0.118	0.016	354.6
	3.50	0.068	0.021	67.9		1.67	0.118	0.016	354.3
	3.50	0.073	0.022	72.6		2.00	0.130	0.017	388.8
	3.50	0.058	0.019	58.1		2.33	0.133	0.017	397.5
	4.00	0.067	0.021	66.8		2.83	0.142	0.018	424.8
	5.25	0.063	0.020	62.7		3.00	0.132	0.017	396.6
	5.75	0.031	0.012	31.4		4.00	0.137	0.018	411.3
6.00	0.030	0.011	29.7	4.00	0.151	0.019	451.8		
F3 $D_b = 2$ mm $D_f = 12$ mm	1.00	0.207	0.033	414.0	4.00	0.139	0.018	418.2	
	1.25	0.138	0.023	276.4	5.00	0.131	0.017	393.9	
	1.25	0.160	0.026	319.4	1.17	0.165	0.033	247.8	
	1.25	0.133	0.023	266.2	1.17	0.087	0.019	131.0	
	1.38	0.101	0.018	202.2	1.67	0.075	0.017	113.1	
	1.38	0.092	0.016	183.2	1.83	0.081	0.018	121.7	
	1.75	0.089	0.016	177.2	2.33	0.097	0.021	145.5	
	1.88	0.091	0.016	182.8	2.50	0.088	0.019	131.3	
	2.13	0.099	0.018	197.6	3.00	0.093	0.020	139.7	
	2.50	0.123	0.021	245.4	3.17	0.093	0.020	139.4	
	3.13	0.126	0.022	252.8	3.50	0.093	0.020	140.1	
	3.13	0.120	0.021	239.0	3.67	0.091	0.020	137.1	
	3.25	0.122	0.021	243.2	4.00	0.101	0.022	150.9	
	3.88	0.119	0.021	238.8	4.33	0.099	0.021	147.8	
	4.13	0.111	0.019	222.2	5.00	0.093	0.020	139.5	
5.63	0.086	0.016	171.8	5.83	0.074	0.017	110.3		
6.13	0.068	0.013	135.6	6.83	0.059	0.014	88.4		